

Physical Properties of Giant Molecular Clouds in the Large Magellanic Cloud

A. Hughes^{1,2*}, T. Wong³, J. Ott⁴, E. Muller⁵, J. L. Pineda^{6†}, Y. Mizuno⁵,
 J.-P. Bernard⁷, D. Paradis⁸, S. Maddison¹, W. T. Reach⁸, L. Staveley-Smith⁹,
 A. Kawamura⁵, M. Meixner^{10,11}, S. Kim¹², T. Onishi^{5,13}, N. Mizuno^{5,14}, Y. Fukui⁵

¹Centre for Supercomputing and Astrophysics, Swinburne University of Technology, Hawthorn VIC 3122, Australia

²CSIRO Australia Telescope National Facility, PO Box 76, Epping NSW 1710, Australia

³Astronomy Department, University of Illinois, 1002 W. Green St, Urbana, IL 61801, USA

⁴National Radio Astronomy Observatory, P.O. Box O, 1003 Lopezville Road, Socorro, NM 87801, USA

⁵Department of Astrophysics, Nagoya University, Furo-cho, Chikusa-ku, Nagoya 464-8602, Japan

⁶Jet Propulsion Laboratory, California Institute of Technology, 4800 Oak Grove Drive, Pasadena, CA 91109-8099, USA

⁷Centre d'Etude Spatiale des Rayonnements, Universite Paul Sabatier, 9 Av du Colonel Roche, BP 44346, Toulouse, France

⁸Spitzer Science Center, Caltech, MS220-6, Pasadena, CA 91125, USA

⁹International Centre for Radio Astronomy Research, M468, University of Western Australia, 35 Stirling Hwy, Crawley, WA 6009

¹⁰Space Telescope Science Institute, 3700 San Martin Drive, Baltimore, MD 21218, USA

¹¹Radio and Geoastronomy Division, Harvard-Smithsonian for Astrophysics, 60 Garden St, MS 42, Cambridge, MA 02138-1516, USA

¹²Department of Astronomy and Space Science, Sejong University, KwangJin-gu, KunJa-dong 98, Seoul 143-747, Korea

¹³Department of Physical Science, Osaka Prefecture University, Gakuen 1-1, Sakai, Osaka 599-8531, Japan

¹⁴ALMA-J Project Office, National Astronomical Observatory of Japan, 2-21-1 Osawa, Mitaka, Tokyo 181-8588, Japan

Typeset 30 May 2018; Received / Accepted

ABSTRACT

The Magellanic Mopra Assessment (MAGMA) is a high angular resolution $^{12}\text{CO}(J = 1 \rightarrow 0)$ mapping survey of giant molecular clouds (GMCs) in the Large and Small Magellanic Clouds using the Mopra Telescope. Here we report on the basic physical properties of 125 GMCs in the Large Magellanic Cloud (LMC) that have been surveyed to date. The observed clouds exhibit scaling relations that are similar to those determined for Galactic GMCs, although LMC clouds have narrower linewidths and lower CO luminosities than Galactic clouds of a similar size. The average mass surface density of the LMC clouds is $50 \text{ M}_{\odot} \text{ pc}^{-2}$, approximately half that of GMCs in the inner Milky Way. We compare the properties of GMCs with and without signs of massive star formation, finding that non-star-forming GMCs have lower peak CO brightness than star-forming GMCs. The average CO-to-H₂ conversion factor, X_{CO} , of non-star-forming GMCs is also ~ 50 per cent larger than for star-forming GMCs. We compare the properties of GMCs with estimates for local interstellar conditions: specifically, we investigate the H I column density, radiation field, stellar mass surface density and the external pressure. Very few cloud properties demonstrate a clear dependence on the environment; the exceptions are significant positive correlations between i) the H I column density and the GMC velocity dispersion, ii) the stellar mass surface density and the average peak CO brightness, and iii) the stellar mass surface density and the CO surface brightness. The molecular mass surface density of GMCs without signs of massive star formation shows no dependence on the local radiation field, which is inconsistent with the photoionization-regulated star formation theory proposed by McKee (1989). We find some evidence that the mass surface density of the MAGMA clouds increases with the interstellar pressure, as proposed by Elmegreen (1989), but the detailed predictions of this model are not fulfilled once estimates for the local radiation field, metallicity and GMC envelope mass are taken into account.

Key words: galaxies: ISM – ISM: molecules – Magellanic Clouds

1 INTRODUCTION

In the Milky Way, molecular gas is mostly located in giant molecular clouds (GMCs) with masses $M > 10^5 M_{\odot}$ (Solomon et al. 1987, henceforth S87). Understanding the physical properties of the GMCs is important because these clouds are the primary sites of star formation: the formation of GMCs and the transformation of molecular gas into stars are key processes in the life cycle of galaxies. Models of galactic evolution typically assume that GMCs are sufficiently similar across different galactic environments that a galaxy’s star formation rate can be parameterised as the product of the GMC formation rate and the star formation efficiency of molecular gas (e.g. Ballesteros-Paredes & Hartmann 2007; Blitz & Rosolowsky 2006). This approach was initially justified by studies of Galactic molecular clouds, which found that the basic physical properties of GMCs in the Milky Way’s disc obeyed well-defined scaling relations, often referred to as “Larson’s laws” (e.g. S87, Larson 1981; Heyer et al. 2001). More recently, considerable effort has been devoted to determining whether GMCs in other galaxies also follow the Larson relations (e.g. Rosolowsky et al. 2003; Rosolowsky & Blitz 2005; Rosolowsky 2007), since empirical evidence that GMC properties are uniform – or at least exhibit well-behaved correlations with a parameter such as metallicity or pressure – would provide valuable information for developing models of star formation and galaxy evolution through cosmic time.

As well as furnishing galaxy evolution models with empirical inputs, studies of extragalactic GMC populations aspire to resolve long-standing questions about the physical processes that are important for the formation and evolution of molecular clouds: are GMCs quasi-equilibrium structures, for example, or transient features in the turbulent interstellar medium? Do all GMCs form stars, and if not, why not? What is the physical origin of Larson’s scaling relations? Although a number of different theories to explain molecular cloud properties and the Larson relations have been proposed (e.g. M89, E89, Chieze 1987; Fleck 1988), there are few extragalactic GMC samples that are comparable to the S87 catalogue, which contains 273 clouds in the Galactic disc between longitudes 8° and 90° , and with radial velocities between -100 and 200 km s^{-1} . The survey of $^{12}\text{CO}(J = 1 \rightarrow 0)$ emission in the LMC by NANTEN (henceforth “the NANTEN survey”) provided the first complete inventory of GMCs in any galaxy (Fukui et al. 2008), but did not resolve molecular cloud structures smaller than $\sim 40 \text{ pc}$ (we adopt 50.1 kpc for the distance to the LMC, e.g. Alves 2004). Thorough testing of the different molecular cloud models will require deep, unbiased wide-field surveys of molecular clouds at high angular resolution across a range of interstellar conditions. Extensive surveys of this kind are only just feasible with current instrumentation, and hence the number of molecular cloud samples that can be used to falsify molecular cloud models remains frustratingly small.

To date, studies of the CO emission in nearby galaxies have concluded that extragalactic GMCs are alike. For a sample of ~ 70 resolved GMCs located in five galaxies (M31, M33, IC10, and the Magellanic Clouds), Blitz et al. (2007) found that extragalactic GMCs not only follow the Galactic Larson relations, but also that different galaxies have similar GMC mass distributions. Similar conclusions were reached by Bolatto et al. (2008, henceforth B08) using a sample of ~ 100 resolved GMCs in twelve galaxies, although these authors noted that molecular clouds in the SMC tend to have low CO luminosities and narrow linewidths compared to GMCs of a similar size in other galaxies. By comparing tracers of star formation and neutral gas on $\sim 1 \text{ kpc}$ scales for galaxies in The HI Nearby Galaxy Survey (THINGS, which does not include the Magellanic Clouds, Walter et al. 2008), Leroy et al. (2008) found that the star-forming efficiency of molecular gas (defined as the star formation rate surface density per unit molecular gas surface density $SFE_{\text{H}_2} \equiv \Sigma_{\text{SFR}}/\Sigma_{\text{H}_2}$) is approximately constant in normal spiral galaxies, $SFE_{\text{H}_2} = 5.25 \pm 2.5 \times 10^{-10} \text{ yr}^{-1}$. As noted by the authors, this result could arise if the star-forming efficiency of an individual GMC is determined by its intrinsic properties, and if the properties of GMCs are independent of their interstellar environment (e.g. Krumholz & McKee 2005). While the existing observational evidence has so far been interpreted in favour of uniform GMC properties, a dependence of GMC properties on the local interstellar environment is by no means ruled out. A constant SFE_{H_2} on kiloparsec scales indicates that the properties of GMC ensembles are alike on those scales; whether this conclusion can be applied to individual GMCs is far less certain. Neither B08 nor Blitz et al. (2007) pursued the origin of the scatter in the extragalactic Larson relations that they observed, moreover, even though the mean GMC mass surface density for the galaxies in their respective samples varies by more than an order of magnitude, and the mass surface densities of the individual GMCs varies between ~ 10 and $1000 M_{\odot} \text{ pc}^{-2}$ (see also Heyer et al. 2008, for evidence that the mass surface density of Milky Way clouds is not constant). A resolved survey of a large number (> 100) of GMCs located in a single nearby galaxy therefore remains valuable, since it eliminates the uncertainties inherent in combining heterogeneous datasets and provides a sample that is large enough to investigate both the average properties and scaling

* E-mail: ahughes@astro.swin.edu.au

† NASA Postdoctoral Program Fellow

relations of an extragalactic GMC population, as well as the dispersion around overall trends and average quantities.

In this paper, we report on some initial results from the Magellanic Mopra Assessment (MAGMA), an ongoing, high-resolution survey of the $^{12}\text{CO}(J = 1 \rightarrow 0)$ emission from molecular clouds in the Magellanic Clouds using the Mopra Telescope. Here we present results from the Large Magellanic Cloud (LMC) only; a description of the molecular clouds surveyed by MAGMA in the Small Magellanic Cloud (SMC) has been presented elsewhere (Muller *et al.*, accepted). While the $^{12}\text{CO}(J = 1 \rightarrow 0)$ emission from molecular gas in the LMC has been the target of extensive mapping with the NANTEN telescope and Swedish-ESO Submillimetre Telescope (SEST), neither project obtained observations that were ideal for studying the Larson relations in the LMC (Fukui *et al.* 2008; Israel *et al.* 2003). The spatial resolution of the NANTEN survey is comparable to the size of a typical Milky Way GMC (~ 50 pc, e.g. Blitz 1993); ideally, we would like to resolve structures on smaller spatial scales in order to include less massive GMCs in our analysis. Resolved observations are crucial, moreover, for accurate estimates of derived GMC quantities such as virial mass and mass surface density. The SEST Key Programme *CO in the Magellanic Clouds* mapped molecular clouds in the LMC with comparable spatial resolution as MAGMA (~ 10 pc), but was strongly biased towards regions associated with well-known sites of active star formation. An analysis of the striking molecular cloud complex situated south of the 30 Doradus star-forming complex using the MAGMA data has already been presented by Ott *et al.* (2008) and Pineda *et al.* (2009); in this paper, we turn our attention to the general LMC cloud population.

This paper is structured as follows: in Section 2, we summarise the MAGMA observing strategy and our data reduction procedure, and also describe the ancillary data that we have used in our analysis. Section 3 outlines the approach that we have used to identify GMCs and to measure their physical properties. In Section 4, we compare the properties of GMCs with and without star formation. Scaling relations between the cloud properties are discussed in Section 5, while Section 6 presents a comparison between the intrinsic physical properties of the GMCs and properties of the local interstellar environment. In Section 7, we discuss whether our results are consistent with i) the photoionization-regulated theory of star formation proposed by McKee (1989, henceforth M89) and ii) a dominant role for interstellar gas pressure in the determination of molecular cloud properties, as suggested by Elmegreen (1989, henceforth E89). We conclude with a summary of our key results in Section 8.

2 DATA

2.1 The MAGMA LMC survey: observations and data reduction

MAGMA observations of the $^{12}\text{CO}(J = 1 \rightarrow 0)$ emission from molecular clouds in the LMC are conducted at the Mopra Telescope, which is situated near Coonabarabran, Australia.¹ At 115 GHz, the Mopra Telescope has a full width at half-maximum (FWHM) beam size of 33 arcsec, corresponding to a spatial resolution of 8 pc at our assumed distance to the LMC. Due to the large angular size of the LMC's gas disc, and the small covering fraction of the $^{12}\text{CO}(J = 1 \rightarrow 0)$ emission (e.g. Mizuno *et al.* 2001), we use the NANTEN survey of Fukui *et al.* (2008) to select regions of bright $^{12}\text{CO}(J = 1 \rightarrow 0)$ emission for high-resolution mapping. MAGMA observations target all molecular clouds with CO luminosities $L_{\text{CO}} > 7000$ K km s⁻¹ pc² and peak integrated intensities > 1 K km s⁻¹ in the NANTEN cloud catalogue of Fukui *et al.* (2008). In combination, these clouds contribute ~ 70 per cent of the LMC's total CO luminosity. An integrated intensity map of the CO emission in the LMC by MAGMA is shown in Fig. 1, with outlines that represent the survey's coverage.

MAGMA observations are conducted in "on-the-fly" (OTF) raster-mapping mode. A grid of 5×5 arcmin² OTF fields is placed over the region surrounding a molecular cloud target. The field centres are separated by 4.75 arcmin in RA and Dec; this 15 arcsec overlap ensures full coverage of the molecular cloud and facilitates mosaicking. In OTF mode, the telescope takes data continuously while scanning across the sky. Along each row of an OTF field, individual spectra are recorded every 14 arcsec, so that the telescope beam is oversampled in the scanning direction. The spacing between rows is 10 arcsec, also oversampling the beam. Each row is preceded by an off-source (emission-free) integration situated approximately 10 to 20 arcmin from the field centre; an absolute location for the OFF spectra was selected for each molecular cloud target in order to ensure a consistent sky subtraction. To minimize scanning artefacts, each field in the final survey dataset is mapped twice: an initial pass is made with the telescope scanning in the RA direction, and a second pass then conducted in the orthogonal direction. The data presented in this paper were obtained during the southern hemisphere winters of 2005 to 2008. Observations are complete for ~ 40 per cent of the clouds presented here; the remaining clouds have been scanned in the RA direction only. The full MAGMA LMC dataset will be presented in a subsequent paper (Wong *et al.*, in preparation).

¹ The Mopra Telescope is managed by the Australia Telescope, which is funded by the Commonwealth of Australia for operation as a National Facility by the CSIRO.

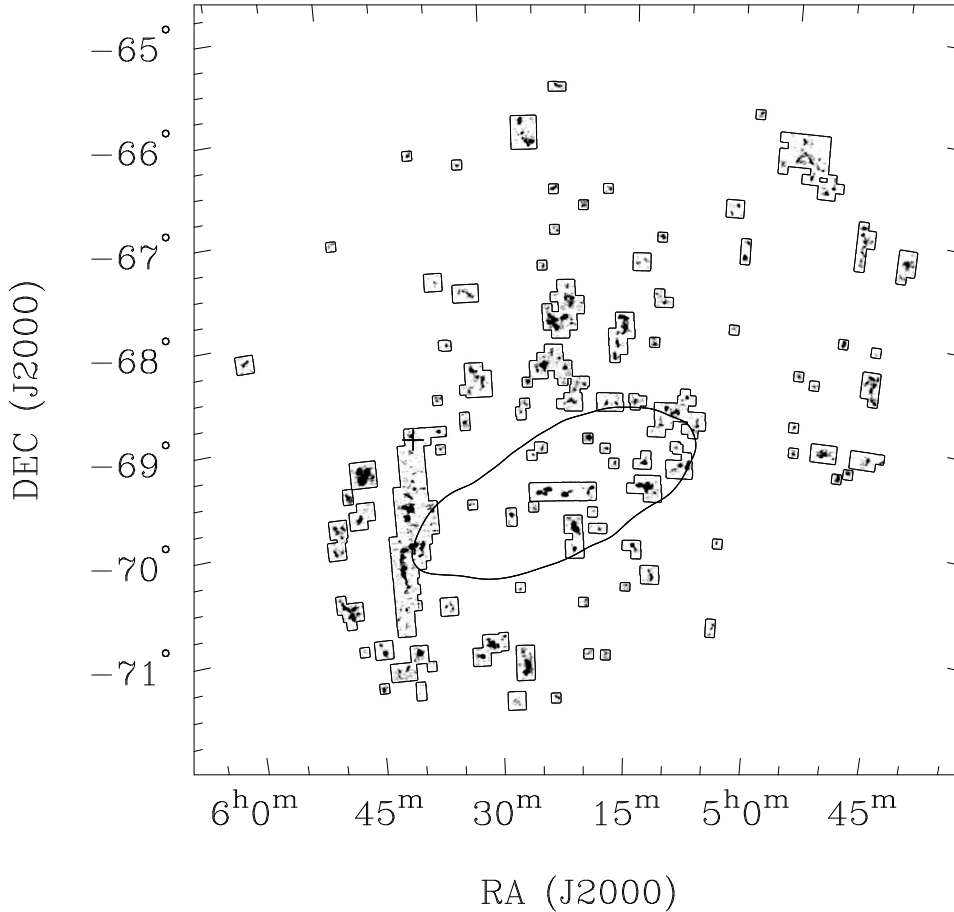


Figure 1. A map of CO integrated intensity in the LMC by MAGMA (greyscale). The thin black lines indicate the coverage of the MAGMA observations included in this paper. The black cross indicates the position of 30 Doradus; in the text, we refer to the large survey region that encloses and extends south from 30 Dor as the “molecular ridge”. The black ellipse indicates where the stellar surface density, Σ_* , is greater than $100 M_{\odot} \text{pc}^{-2}$; we refer to this region in the text as the “stellar bar”.

A system temperature measurement is obtained with an ambient load at the start of each OTF map and every 20 to 30 minutes thereafter. In the interval between these measurements, the system temperature is monitored using a noise diode. Typical system temperatures for the survey observations are between 500 and 600 K; observing is abandoned when system temperatures exceed ~ 1000 K. Our intention is to obtain data with uniform sensitivity, so OTF fields with average system temperatures above ~ 850 K are re-observed. Between each OTF map, the pointing of the antenna is verified by observing the nearby SiO maser RDor. The pointing solution is updated (and re-verified) if the pointing error in azimuth or elevation is greater than 8 arcsec. Prior to correction, the pointing errors are typically below 10 arcsec.

In 2005, the Mopra Telescope was equipped with a dual polarisation SIS receiver that produced 600 MHz instantaneous bandwidth for observing frequencies between 86 and 115 GHz (Moorey et al. 1997). The correlator at that time could be configured for bandwidths between 4 and 256 MHz across the receiver’s 600 MHz band (Wilson et al. 1992). Our 2005 observations targeted the molecular ridge region discussed by Ott et al. (2008) and Pineda et al. (2009) (see Fig. 1), with some data obtained for additional fields near RA 05h16m, Dec -68d10m (J2000) and RA 05h24m, Dec -69d40m (J2000) (J2000). For all 2005 observations, the correlator was configured with 1024 channels over a 64 MHz bandwidth centred on 115.16 MHz, which provided a velocity resolution of 0.16 km s^{-1} per channel across a reliable velocity bandwidth of $\sim 120 \text{ km s}^{-1}$. As this is not quite sufficient to cover the total radial velocity range of the LMC’s CO emission, the centre of the observing band was placed near the peak of CO spectrum obtained by NANTEN for the region being observed. In subsequent years, the data were recorded using the newly installed MMIC receiver and the University of New South Wales Digital Filter Bank (MOPS).² In the narrowband configuration used for the MAGMA survey observations, MOPS can simultaneously record dual polarisation

² The University of New South Wales Digital Filter Bank used for the observations with the Mopra Telescope was provided with support from the Australian Research Council.

data for up to sixteen 138 MHz windows situated within an 8 GHz band. Each 138 MHz window is divided into 4096 channels; for our survey observations at 115 GHz, this configuration provides a velocity resolution of 0.09 km s^{-1} per channel across the velocity range $[90,410] \text{ km s}^{-1}$.

The Mopra beam has been described by Ladd et al. (2005). These authors identify three components - the 'main beam', and the inner and outer 'error beams' - that contribute to the antenna response. The presence of these non-negligible error beams implies that the telescope efficiency, η , will depend on source size. In the 2004 observing season, Ladd et al. (2005) derived a main-beam efficiency factor of $\eta_{\text{mb}} = 0.42$ for observations at 115 GHz, and an 'extended' beam efficiency of $\eta_{\text{xb}} = 0.55$ for sources that are comparable to the size of the inner error beam ($\sim 80 \text{ arcsec}$). For clouds in the MAGMA survey, we consider the extended beam efficiency factor to be more appropriate.

To monitor the reliability of the flux calibration, we observed the standard source Orion KL (RA 05h35m14.5s, Dec -05d22m29.56s (J2000)) once per observing session throughout our survey. In 2005, we measured an average peak brightness temperature of Orion KL of $55 \pm 3 \text{ K}$ (in T_A^* units). According to the SEST documentation,³ the peak antenna temperature of Orion KL is $T_A^* \sim 71 \text{ K}$, corresponding to a main beam temperature of $T_{\text{mb}} \sim 102 \text{ K}$ for an efficiency factor of $\eta_{\text{mb}} = 0.7$ (Johansson et al. 1998). This suggests that data from the two telescopes can be placed on the same brightness temperature scale using a factor of $\eta_{\text{xb}} = 0.54 \pm 0.03$ for the Mopra data, in excellent agreement with the telescope efficiency derived by Ladd et al. (2005). In subsequent years, the average peak brightness temperature that we have measured for Orion KL has varied. In 2006, we measured an average peak brightness temperature of $35 \pm 4 \text{ K}$, while our average measurements in 2007 and 2008 were $43 \pm 3 \text{ K}$ and $50 \pm 3 \text{ K}$ respectively. For these data, we therefore used conversion factors of 0.35 (2006), 0.43 (2007) and 0.49 (2008). To validate the final flux scale of our Mopra data, we compiled published SEST measurements of LMC molecular clouds from the studies by Israel et al. (1993), Chin et al. (1997), Kutner et al. (1997), Johansson et al. (1998) and Israel et al. (2003). We were able to compare Mopra and SEST measurements of the peak brightness and peak integrated intensity for 40 clouds. For both the peak brightness and the peak integrated intensity of these clouds, the average ratio between the SEST and Mopra measurements was 1.1, with a dispersion of ~ 20 per cent.

The processing of the survey data involved four main steps. An initial correction to align the position and time stamp information in the raw data files was applied to data obtained in 2005, using the `mopfix` task of the MIRIAD software package (Sault et al. 1995). Bandpass calibration and baseline-fitting were performed using the AIPS++ LIVEDATA package. LIVEDATA determines the bandpass calibration for each row of an OTF map using the preceding OFF scan and then fits a user-specified polynomial to the spectral baseline. We chose to fit the spectral baselines with a first-order polynomial: data subcubes containing baselines showing higher order ripples were rejected. The spectra were combined to form a spectral line cube using the AIPS++ GRIDZILLA package. Each (x, y, v) cell within the final cube is sampled multiple times by the OTF scans: GRIDZILLA averages the spectra contributing to the emission within each cell according to a convolution kernel, beam profile and weighting scheme specified by the user. We chose to grid the data with a cell size of $9 \times 9 \text{ arcsec}^2$, aggregating the data from both polarisations and both scanning directions. The data were weighted by the inverse of the system temperature measurements. We used a truncated Gaussian convolution kernel with a FWHM of 1 arcmin and a cutoff radius of 30 arcsec, producing an output data subcube with effective angular resolution of 45 arcsec. Although GRIDZILLA can process data from contiguous OTF fields, it cannot process data recorded with different correlator configurations simultaneously. The data subcubes from different years were thus processed separately, and were converted to T_{mb} units using the annual extended beam efficiency factors derived from our Orion KL observations. The MIRIAD task `imcomb`, which weights the input data by the inverse of the RMS noise, was then used to combine data from regions that were observed over multiple observing seasons. Finally, in order to increase the signal-to-noise (S/N), we binned the MAGMA data subcubes to a velocity resolution of 0.53 km s^{-1} and smoothed them to an angular resolution of 1 arcmin. The average RMS noise in these subcubes is 0.24 K per 0.53 km s^{-1} channel. An example of the integrated $^{12}\text{CO}(J = 1 \rightarrow 0)$ emission for one such MAGMA subcube is shown in Fig. 2.

2.2 Ancillary data

2.2.1 H I data

To trace the atomic gas in the LMC, we use the H I map published by Kim et al. (2003), which combines data from the Australia Telescope Compact Array (ATCA Kim et al. 1998) and the Parkes single-dish telescope (Staveley-Smith et al. 2003). The angular resolution of the H I data is 1 arcmin, well-matched to the reduced MAGMA CO data. The H I data cube has a velocity resolution of 1.65 km s^{-1} , with a column density sensitivity of $7.2 \times 10^{18} \text{ cm}^{-2}$ per channel. We construct an

³ <http://www.apex-telescope.org/sest/html/telescope-calibration/calib-sources/orionkl.html>

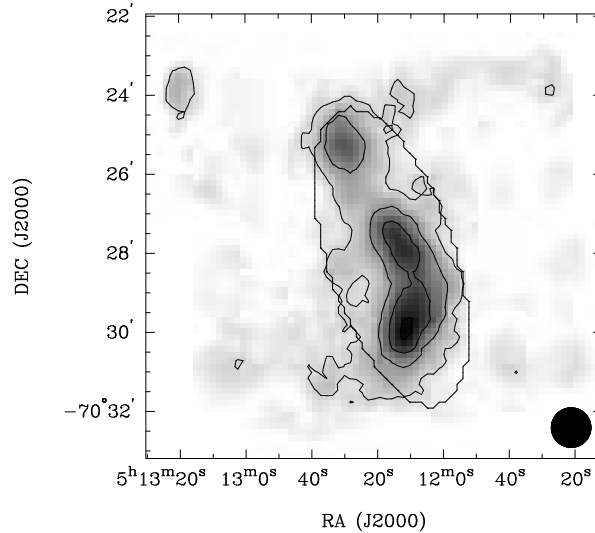


Figure 2. A $^{12}\text{CO}(J = 1 \rightarrow 0)$ integrated intensity map of an example GMC in the MAGMA cloud list. The contour spacing is 2 km s^{-1} , with the lowest contour at $I_{\text{CO}} = 1.5 \text{ km s}^{-1}$. The ellipse represents the fit derived by CPROPS, from which the major and minor axis and position angle of the GMC were taken. As explained in Section 3, we are interested to identify GMCs in the MAGMA data subcubes, rather than structure on smaller scales corresponding to the spatial resolution of the survey. The black circle in the lower right corner represents the Mopra beam.

H I integrated intensity emission map of the LMC, I_{HI} , by integrating the H I data cube over the heliocentric velocity range 196 to 353 km s^{-1} . We assume that the H I emission is optically thin everywhere, and derive a map of the LMC’s H I column density, $N(\text{HI})$, according to

$$N(\text{HI})[\text{cm}^{-2}] = 1.82 \times 10^{18} I_{\text{HI}}[\text{K km s}^{-1}]. \quad (1)$$

Our estimate for $N(\text{HI})$ is likely to be a lower limit since the H I emission in the LMC may have significant optical depth, especially along the sightlines towards molecular clouds (Dickey et al. 1994; Marx-Zimmer et al. 2000; Bernard et al. 2008, see also Section 7.2.2).

2.2.2 Stellar mass surface density

To trace the mass distribution within the LMC’s stellar disc, we use the stellar mass surface density map presented in fig. 1c of Yang et al. (2007). The map is based on number counts of red giant branch (RGB) and asymptotic giant branch (AGB) stars, selected by their colours from the Two Micron All Sky Survey Point Source Catalogue (Skrutskie et al. 2006). The star counts are binned into $40 \text{ pc} \times 40 \text{ pc}$ pixels, and then convolved with a Gaussian smoothing kernel with $\sigma = 100 \text{ pc}$. The resulting map is normalized to a measure of absolute stellar mass surface density by adopting a total stellar mass for the LMC of $2 \times 10^9 M_{\odot}$ (Kim et al. 1998). The resolution of the stellar surface density map is considerably coarser than the angular resolution of our MAGMA data subcubes, so it is possible that the average stellar mass surface density of smaller GMCs is underestimated due to beam dilution. RGB and AGB stars are relatively old populations, however, so their spatial distribution is likely to be smooth. In particular, we do not expect them to be strongly clustered in the vicinity of molecular clouds (e.g. Nikolaev & Weinberg 2000).

2.2.3 Interstellar radiation field

To estimate the interstellar radiation field at the locations of molecular clouds within the LMC, we use the dust temperature (T_d) map presented in fig. 7 of Bernard et al. (2008). The map is derived using the ratio of the IRIS $100 \mu\text{m}$ and *Spitzer* $160 \mu\text{m}$ emission maps (Miville-Deschênes & Lagache 2005; Meixner et al. 2006), assuming that dust emission can be modelled as a grey body:

$$I_{\nu} \propto \nu^{\beta} B_{\nu}(T_d), \quad (2)$$

with $\beta = 2$ at far-infrared wavelengths.⁴ Bernard et al. (2008) find that dust temperatures in the LMC vary from 12 K up to 34.7 K, with an average value of 18.3 K. This is significantly colder than previous determinations, especially for estimates that attempted to constrain the dust temperature using the *IRAS* 60 μ m flux density. As noted by Bernard et al. (2008), emission at 60 μ m is highly contaminated by out-of-equilibrium emission from very small grains (VSGs), and this is especially true in the LMC, due to the presence of excess 70 μ m emission. Temperatures derived from the *IRAS* 60/100 μ m flux density ratio may therefore be strongly overestimated.

For dust grains in thermal equilibrium, the strength of the radiation field, G_0 , is related to the dust temperature by $G_0 \propto T_d^{4+\beta}$ (e.g. Lequeux 2005). The average strength of G_0 across the entire LMC is thus only a factor of ~ 1.3 greater than in the solar neighbourhood, $G_{0,\odot}$, where the dust temperature is 17.5 K (with $\beta = 2$, Boulanger et al. 1996). At the locations observed by MAGMA, $G_0/G_{0,\odot}$ varies between 0.5 and 58.8, with a median value of 1.7. For $G_0/G_{0,\odot}$ averaged over the projected cloud areas, we obtain values in the range 0.5 to 8.0. Our derived value for the strength of the radiation field near the well-known LMC star-forming region N159W ($G_0/G_{0,\odot} = 8.4$) is very low compared to the value obtained by previous estimates (e.g. Israel et al. 1996; Pineda et al. 2008, 2009). Part of the discrepancy may be due to beam dilution since the resolution of the Bernard et al. (2008) dust temperature map is 4 arcmin, which corresponds to a spatial scale of 60 pc in the LMC. However, we also note that our method for determining $G_0/G_{0,\odot}$ is extremely sensitive to the assumed dust temperature, which is colder than reported by previous analyses. At the locations of the molecular clouds in the Bernard et al. (2008) dust temperature map, the mean (maximum) formal error on T_d is 2 per cent (12 per cent). These errors do not include potential variations in the value of β , however, so the true uncertainty is likely to be greater than this. Despite the uncertainties regarding the absolute value of $G_0/G_{0,\odot}$, we emphasise that our analysis concerns the relationship between GMC properties and the relative strength of the radiation field, and our conclusions do not rely on an absolute calibration of $G_0/G_{0,\odot}$. Finally, we note that while the resolution of the Bernard et al. (2008) dust temperature map is coarser than the angular resolution of our MAGMA CO data, it is still likely to provide a reasonable estimate for the average dust temperature within individual GMCs with $R \geq 30$ pc. For smaller clouds, the average dust temperature and average radiation field may be underestimated due to beam dilution.

3 MEASURING GMC PROPERTIES

To identify GMCs in the MAGMA data subcubes and measure their properties, we have used the algorithms presented in Rosolowsky & Leroy (2006, implemented in IDL as part of the CPROPS package). CPROPS uses a dilated mask technique to isolate regions of significant emission within spectral line cubes, and a modified watershed algorithm to assign the emission into individual clouds. Moments of the emission along the spatial and spectral axes are used to determine the size, linewidth and flux of the clouds, and optional corrections for the finite sensitivity and instrumental resolution may be applied to the measured cloud properties. Each step of the CPROPS method is described in detail by Rosolowsky & Leroy (2006).

Regions of significant emission within the MAGMA data subcubes are initially identified by finding pixels with emission greater than a threshold of $4\sigma_{RMS}$ across two contiguous velocity channels. The mask around these core regions is then expanded to include all the pixels connected to the core with emission greater $1.5\sigma_{RMS}$ across at least two consecutive channels. We explored a range of values for the threshold and edge parameters in the masking process, and found that these values distinguished credible emission regions (i.e. the mask did not expand excessively into the noise) and also yielded reliable measurements for the properties of faint clouds. The emission identified with an isolated cloud in the MAGMA dataset is illustrated in Fig. 3.

Once regions of significant emission have been identified, CPROPS assigns the emission to individual cloud structures. To generate the preliminary list of GMC candidates, we used the default parameters for the identification of GMCs that are recommended in Rosolowsky & Leroy (2006). In this case, the parameters of the decomposition are motivated by the observed physical properties of Galactic GMCs: spatial sizes greater than ~ 10 pc, linewidths of several km s^{-1} , and brightness temperatures less than ~ 10 K. We adopt this approach because our goal is to describe the properties of GMCs in the LMC and to investigate how these properties might differ to the properties of GMCs in other galaxies. As noted by Rosolowsky & Leroy (2006), GMCs contain structure across a wide range of size scales, so identifying the clumpy substructure – with a size scale of ~ 1 pc and typical linewidth of $\sim 1 \text{ km s}^{-1}$ – within the clouds in our spectral line cubes would require different decomposition parameters than the ones that we have used. While the properties and scaling relations of this substructure is an important topic for investigation, we defer this analysis to a future paper. A previous analysis of the MAGMA data in the molecular ridge region employed a different decomposition algorithm (i.e. GAUSSCLUMPS, Pineda et al. 2009), which identified structures

⁴ 'IRIS' is an abbreviation for Improved Reprocessing of the *IRAS* Survey. As described in Miville-Deschênes & Lagache (2005), IRIS images have improved zodiacal light subtraction, absolute calibration and scanning stripe suppression than the *IRAS* Sky Survey images.

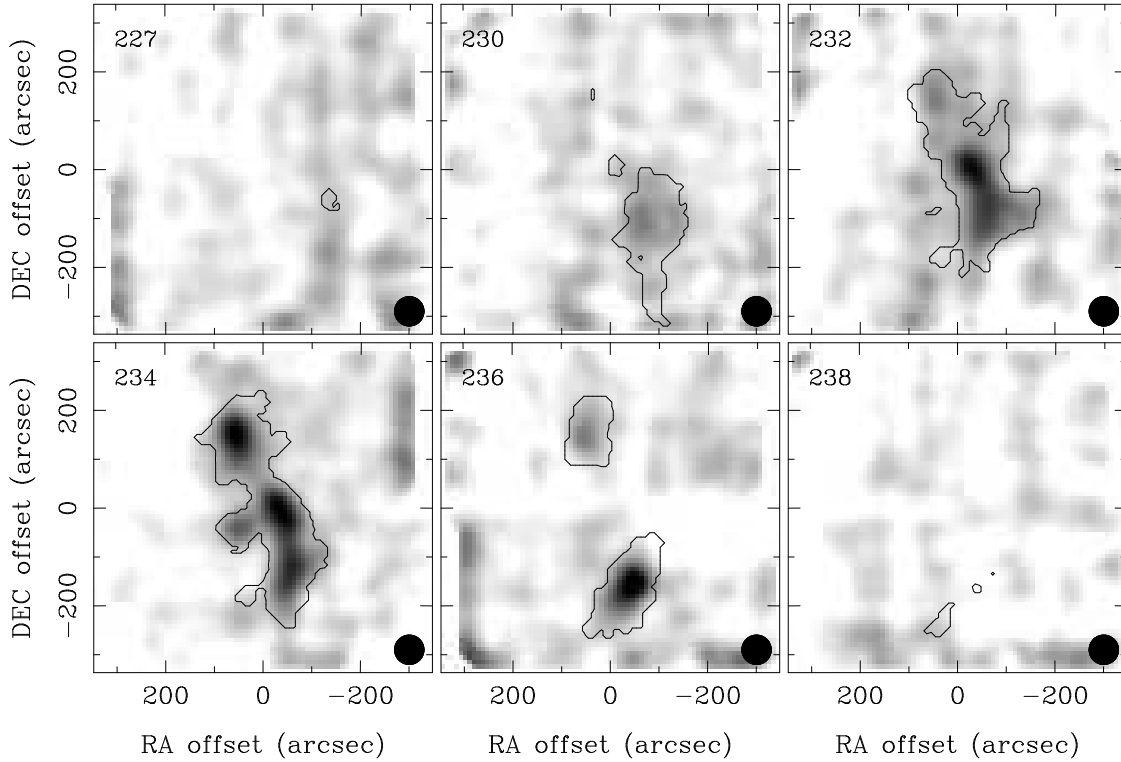


Figure 3. Channel maps of the CO emission from the GMC in Fig. 2 (greyscale). The black contour indicates the emission region that CPROPS identifies as belonging to the cloud. The velocity axis of the MAGMA data subcube and CPROPS assignment cube has been binned to a channel width of 2.1 km s^{-1} for illustration only. The black circle in the lower right corner of each panel represents the Mopra beam.

that are typically smaller (with radii between 6 and 20 pc) than the GMCs described here.

Our initial list of GMC candidates contained 237 objects. After cross-checking the CPROPS cloud identifications against the NANTEN $^{12}\text{CO}(J = 1 \rightarrow 0)$ data cube and the MAGMA data subcubes to verify that the identified objects were genuine, we rejected 54 features that were clearly noise peaks or map edge artefacts. To ensure that the properties of clouds in our final list are reliable, we impose a signal-to-noise threshold $S/N \geq 5$ and reject objects with measurement errors for the radius and velocity dispersion that are greater than 20 per cent. We further require that CPROPS is able to apply the corrections for sensitivity and instrumental resolution successfully (i.e. these corrections do not result in undefined values). The resulting sample of GMCs, which we refer to as the “MAGMA cloud list”, contains 125 clouds. To verify the results of our analysis, we also define a “high quality” GMC sample, which contains 57 clouds with $S/N \geq 9$ and for which the uncertainties in the radius and velocity dispersion measurements are less than 15 per cent.

Cloud properties follow the standard CPROPS definitions. The cloud radius is defined as $R = 1.91\sigma_R$, where σ_R is the geometric mean of the second moments of the emission along the cloud’s major and minor axes. The velocity dispersion, σ_v , is the second moment of the emission distribution along the velocity axis, which for a Gaussian line profile is related to the FWHM linewidth, Δv , by $\Delta v = \sqrt{8 \ln 2} \sigma_v$ (e.g. Rosolowsky & Leroy 2006). The CO luminosity of the cloud, L_{CO} , is simply the emission inside the cloud integrated over position and velocity, i.e.

$$L_{\text{CO}}(\text{K km s}^{-1} \text{ pc}^2) = D^2 \left(\frac{\pi}{180 \times 3600} \right)^2 \Sigma T_i \delta v \delta x \delta y \quad (3)$$

where D is the distance to the LMC in parsecs, δx and δy are the spatial dimensions of a pixel in arcseconds, and δv is the width of one channel in km s^{-1} . The virial mass is given by $M_{\text{vir}} = 1040\sigma_v^2 R M_{\odot}$, which assumes that molecular clouds are spherical with $\rho \propto r^{-1}$ density profiles (MacLaren et al. 1988). CPROPS estimates the error associated with a cloud property measurement using a bootstrapping method, which is described in section 2.5 of Rosolowsky & Leroy (2006).

In addition to the basic properties reported by CPROPS, we define the CO surface brightness as the total CO luminosity of a cloud divided by its area, $I_{\text{CO}}[\text{K km s}^{-1}] \equiv L_{\text{CO}}/\pi R^2$. The molecular mass surface density, Σ_{H_2} , is defined as the virial

mass divided by the cloud area, $\Sigma_{\text{H}_2} [\text{M}_\odot \text{pc}^{-2}] \equiv M_{\text{vir}}/\pi R^2$. The CO-to-H₂ conversion factor, X_{CO} , may be expressed as the ratio between these quantities: $X_{\text{CO}} [\text{cm}^{-2} (\text{K km s}^{-1})^{-1}] \equiv \Sigma_{\text{H}_2} [\text{M}_\odot \text{pc}^{-2}] / (2.2 I_{\text{CO}} [\text{K km s}^{-1}])$. We note that our definitions of X_{CO} and Σ_{H_2} assume that GMCs manage to achieve dynamic equilibrium: if the degree of virialisation is not constant for LMC molecular clouds, then variations in X_{CO} and Σ_{H_2} may instead reflect differences between the dynamical state of the clouds. We estimate the uncertainties in X_{CO} , I_{CO} and Σ_{H_2} using standard error propagation rules.

As emphasized by Rosolowsky & Leroy (2006), the resolution and sensitivity of a dataset influence the derived cloud properties. In order to reduce these observational biases, they recommend extrapolating the cloud property measurements to values that would be expected in the limiting case of perfect sensitivity (i.e. a brightness temperature threshold of 0 K), and correcting for finite resolution in the spatial and spectral domains by deconvolving the telescope beam from the measured cloud size, and deconvolving the channel width from the measured linewidth. The procedures that CPROPS uses to apply these corrections are described in Rosolowsky & Leroy (2006, see especially fig. 2 and sections 2.2 and 2.3). For the analysis in this paper, we use cloud property measurements that have been corrected for resolution and sensitivity bias.

The GMCs observed by MAGMA in the LMC have radii ranging between 13 and 160 pc, velocity dispersions between 1.0 and 6.1 km s⁻¹, peak CO brightnesses between 1.2 and 7.1 K, CO luminosities between 10^{3.5} and 10^{5.5} K km s⁻¹ pc², and virial masses between 10^{4.2} and 10^{6.8} M_⊙. The clouds tend to be elongated, with a median axis ratio of 1.7. A detailed analysis of the cloud property distributions and their uncertainties will be presented once the MAGMA LMC survey is complete (Wong *et al.*, in preparation).

4 PHYSICAL PROPERTIES OF NON-STAR-FORMING GMCs

Molecular clouds have traditionally been modelled as quasi-equilibrium structures, but recent theoretical work has also begun to explore whether molecular clouds might form and disperse more rapidly as a consequence of large-scale dynamical events in the ISM, such as turbulent flows or cloud collisions (e.g. Bergin *et al.* 2004; Tasker & Tan 2008). Observational constraints on the physical properties of recently formed GMCs would be a useful contribution to the debate about GMC lifetimes, but it remains unclear whether observations of ¹²CO($J = 1 \rightarrow 0$) emission alone can distinguish between younger and more evolved GMCs. While it is plausible that some potential characteristics of newly formed GMCs, such as colder gas temperatures, stronger bulk motions or sparser CO filling factors, would have observational signatures, it is also possible that the onset of widespread ¹²CO($J = 1 \rightarrow 0$) emission might occur late in the cloud formation process, or that physical conditions in the CO-emitting regions of GMCs are relatively uniform and therefore insensitive to a cloud’s evolutionary state. In this section, we investigate whether there are significant differences between the properties of young GMC candidates and other GMCs in the MAGMA LMC cloud list.

We constructed a sample of young GMC candidates using the evolutionary classification scheme designed by Kawamura *et al.* (2009) for the 272 GMCs in the NANTEN LMC catalogue (Fukui *et al.* 2008). Kawamura *et al.* (2009) classified GMCs on the basis of their association with H II regions and young stellar clusters, finding 72 Type I GMCs that show no association with massive star-forming phenomena. An important assumption behind this approach is that all GMCs eventually form stars and are finally dissipated by their stellar offspring; in this scenario, GMCs without signs of massive star formation may be considered young. To date, MAGMA has observed 30 Type I NANTEN GMCs, but there are only 17 MAGMA clouds associated with these Type I GMCs that satisfy our criteria for inclusion in the MAGMA cloud list: henceforth, we refer to these 17 MAGMA clouds as the “young GMC sample” or the “non-star-forming GMCs”. The 17 clouds in the young GMC sample correspond to 16 NANTEN GMCs: 15 of the 17 MAGMA clouds demonstrate a one-to-one correspondence with a Type I GMC in the NANTEN catalogue, while the other NANTEN GMC divides into two clouds at MAGMA’s finer resolution. CPROPS identifies 10 more objects in the MAGMA data subcubes that are associated with a further 8 NANTEN Type I GMCs, but these objects either have $S/N < 5$ and/or measurement errors that exceed 20 per cent, and are therefore excluded from the MAGMA cloud list. CPROPS does not identify any significant emission in the MAGMA data subcubes for the remaining six NANTEN Type I GMCs that we have observed to date, although we note that these are all regions of the MAGMA survey that have only been scanned once. We do not attempt to re-classify the MAGMA clouds according to the criteria developed by Kawamura *et al.* (2009), but simply ascribe the evolutionary classification of the NANTEN GMC to any MAGMA cloud that is coincident in space and velocity. This classification should be reliable for clouds in the young GMC sample since their projected areas are always smaller than, and contained within, the corresponding NANTEN GMC boundary.

To verify that differences between the properties of star-forming and non-star-forming GMCs are not due solely to variations in the cloud size, we constructed a control sample with the same size distribution as the young GMC sample by matching each of the 17 young GMC candidates with three star-forming clouds in the MAGMA cloud list of a similar radius (i.e.

Table 1. Average physical properties of the MAGMA clouds and results of the KS tests for the young GMC sample. Columns 2 to 4 list the median and median absolute deviation of the properties of clouds in the MAGMA cloud list, the young GMC sample and the control sample respectively. Column 5 lists the median P value obtained in the error trials, and column 6 lists the standard deviation of the P values in the trials (see text).

Cloud Property	MAGMA	Young GMCs	Control	$\langle P \rangle$	$\sigma(P)$
R (pc)	28±8	30±8	30±7	0.96	0.05
σ_v (km s ⁻¹)	2.3±0.5	2.4±0.7	2.1±0.5	0.54	0.18
$\langle T_{\text{pk}} \rangle$ (K)	1.1±0.1	1.0±0.1	1.1±0.1	0.007	0.007
T_{max} (K)	2.2±0.4	1.7±0.2	2.3±0.4	0.003	0.003
L_{CO} (10 ⁴ K km s ⁻¹ pc ²)	1.2±0.6	1.2±0.5	1.2±0.5	0.89	0.11
M_{vir} (10 ⁵ M _⊙)	1.5±0.9	1.7±1.0	1.5±0.8	0.78	0.18
Axis Ratio, Γ	1.7±0.4	1.5±0.2	1.8±0.4	0.25	0.10
Σ_{H_2} (M _⊙ pc ⁻²)	55±22	73±21	52±23	0.13	0.10
I_{CO} (K km s ⁻¹)	4.8±1.5	4.3±0.8	4.6±1.3	0.78	0.15
X_{CO} (cm ⁻² (K km s ⁻¹) ⁻¹)	4.7±1.6	6.9±2.3	5.4±2.0	0.06	0.05
V_{LSR} (km s ⁻¹)	255±22	248±18	256±23	0.18	0.00
R_{gal} (kpc)	1.8±0.9	2.3±0.9	1.8±0.8	0.43	0.00
$N(\text{HI})$ (×10 ²¹ cm ⁻²)	2.7±0.7	2.7±0.4	2.7±0.7	0.66	0.18
Σ_* (M _⊙ pc ⁻²)	48±24	50±16	42±19	0.25	0.10
$G_0/G_{0,\odot}$	1.7±0.5	1.3±0.5	2.0±0.6	0.003	0.003
$\langle T_{\text{pk}}(\text{HI}) \rangle$ (K)	68±10	51±10	68±8	0.0001	0.0001
P_h/k_B (10 ⁴ K cm ⁻³)	6.4±2.5	6.4±0.9	5.54±2.1	0.54	0.18

the control sample contains 51 clouds). Kawamura et al. (2009) found that young GMCs in the NANTEN catalogue tend to be smaller than star-forming GMCs, but here we wish to determine whether there are differences between star-forming and non-star-forming GMCs that persist even after variations in cloud size are suppressed. The average discrepancy between the radius of a young GMC candidates and their three corresponding control clouds was 2 per cent, with a maximum discrepancy of 8 per cent. The average properties of GMCs in the MAGMA cloud list, the young GMC sample and the control sample are listed in Table 1.

To test whether young GMCs have distinct physical properties, we conducted Kolmogorov-Smirnov (KS) tests between the young GMC sample and the control sample. The KS test is a non-parametric test that compares the cumulative distribution functions of two samples in order to determine whether there is a statistically significant difference between the two populations. The test is reliable when the effective number of data points, $N_e \equiv \frac{N_1 N_2}{N_1 + N_2}$, is greater than 4, where N_1 and N_2 are the number of data points in the first and second samples. The result of the KS test can be expressed as a probability, P , that the sample distributions are drawn from the same underlying distribution. As the traditional KS test does not account for uncertainties in the measurements of the cloud properties, we performed 1000 trials of each KS test. For each trial, the value of each cloud property measurement was displaced by $k\Delta x$, where Δx is the absolute uncertainty in the cloud property measurement and k is a uniformly distributed random number between -1 and 1. A summary of the KS test results is shown in Table 1. If the results of the error trials are narrowly distributed around zero – i.e. if $\langle P \rangle \leq 0.05$ and $\sigma(P) \leq 0.05$, where σ represents the standard deviation – we consider that there is statistically significant evidence against the null hypothesis that the cloud samples are drawn from the same underlying population.

Table 1 shows that the properties of both the young GMC and the control sample show a large dispersion around their average value, and that differences between the samples are not always obvious from measures of central tendency. The results of the KS tests indicate that the null hypothesis cannot be rejected for many of the intrinsic cloud properties. Both the maximum peak CO brightness within a GMC (T_{max}) and the average peak CO brightness ($\langle T_{\text{pk}} \rangle$, i.e. the peak CO intensity at the line centre for all independent sightlines through the cloud, averaged over the projected cloud area) tend to be lower for young GMCs. There is no significant difference between the distributions of the total CO luminosity (L_{CO}) or CO surface brightness (I_{CO}) however. The median X_{CO} value for the young GMC sample ($\langle X_{\text{CO}} \rangle = 6.9 \times 10^{20}$ cm⁻² (K km s⁻¹)⁻¹) is ~ 50 per cent greater than the median X_{CO} value for the entire MAGMA LMC cloud list. Some of this variation may be due to cloud size, since the discrepancy is reduced once we restrict our comparison to the control sample. The KS test results indicate that the difference is only marginally significant.

For properties of the local interstellar environment, young GMCs appear to be distributed throughout the LMC in a similar fashion as star-forming GMCs (i.e. across a similar range of galactocentric radii and radial velocities), and they are detected across a comparable range of stellar mass surface densities and H I column densities. There is a clear trend, however, for young GMCs to be located in regions where the H I peak brightness ($\langle T_{\text{pk}}(\text{HI}) \rangle$) is relatively low, and the radiation field (G_0) is

relatively weak. In Section 7.1, we argue that the latter reflects the fact that young massive stars are an important source of dust heating in LMC molecular clouds.

5 CLOUD SCALING RELATIONS

Empirical scaling relations between the basic physical properties of molecular clouds have become a standard test for potential differences between molecular cloud populations. Larson’s initial work identified the three well-known “laws” obeyed by Galactic molecular clouds: i) a power-law relationship between the size of a cloud and its velocity dispersion, ii) a nearly linear correlation between the virial mass of a cloud and mass estimates based on molecular line tracers of H_2 column density, which seemed to imply that molecular clouds are self-gravitating and in approximate virial balance, and iii) an inverse relationship between the size of a cloud and its average density (Larson 1979, 1981). S87 were subsequently able to measure the coefficients and exponents of the power-law relationships between the properties of 273 GMCs in the inner Milky Way, establishing the empirical expressions for Larson’s Laws that have become the yardstick for studies of GMCs in other galaxies and in different interstellar environments (see e.g. B08, Blitz et al. 2007).

Most famously, the analysis by S87 showed that inner Milky Way clouds follow a size-linewidth relation of the form $\sigma_v = 0.72R^{0.5 \pm 0.05} \text{ km s}^{-1}$, and that there is a strong, approximately linear correlation between the clouds’ virial mass and their CO luminosity, $M_{\text{vir}} = 39L_{\text{CO}}^{0.81 \pm 0.03} M_{\odot}$. These two relations can be combined to provide expressions for the relationship between a cloud’s luminosity and size, and luminosity and linewidth: $L_{\text{CO}} \approx 25R^{2.5} \text{ K km s}^{-1} \text{ pc}^{-2}$ and $L_{\text{CO}} \approx 130\sigma_v^5 \text{ K km s}^{-1} \text{ pc}^{-2}$. As noted by S87, clouds in gravitational equilibrium ($M \propto R\sigma_v^2$) with $\sigma_v \propto R^{0.5}$ will follow a mass-size relation of the form $M \propto R^2$. This implies constant average mass surface density for molecular clouds, $\langle \Sigma_{\text{H}_2} \rangle$, which is related to the coefficient of the size-linewidth relation, $C_0 \equiv \sigma_v/\sqrt{R}$, via $\langle \Sigma_{\text{H}_2} \rangle \approx 331C_0^2 M_{\odot} \text{ pc}^{-2}$ for the cloud density profile that we have adopted. S87 found $C_0 = 0.72 \text{ km s}^{-1} \text{ pc}^{-0.5}$ and $\langle \Sigma_{\text{H}_2} \rangle \sim 170 M_{\odot} \text{ pc}^{-2}$ for molecular clouds in the inner Milky Way, slightly higher than the median surface density of the extragalactic GMCs analysed by B08 ($\langle \Sigma_{\text{H}_2} \rangle \sim 130 M_{\odot} \text{ pc}^{-2}$). Heyer et al. (2008) have recently argued that the S87 estimate should be revised downwards to $\sim 100 M_{\odot} \text{ pc}^{-2}$, and we adopt this as our reference value in Figs. 4 to 8.

5.1 The size-linewidth relation

Fig. 4[a] presents a plot of velocity dispersion versus radius for GMCs in the MAGMA cloud list. The LMC clouds are clearly offset towards lower velocity dispersions compared to the $R - \sigma_v$ relations derived by S87 and B08; some of the larger LMC clouds fall under the $R - \sigma_v$ relation determined by B08 ($\sigma_v \approx 0.44_{-0.13}^{+0.18} R^{0.6 \pm 0.1}$) by a factor of ~ 3 in velocity dispersion. The discrepancy between the LMC clouds and the $R - \sigma_v$ relation derived by B08 should not be the result of cloud decomposition techniques, as we have identified cloud and parameterized GMC properties using the same algorithms as these authors. In the turbulent paradigm, the offset towards lower velocity dispersion at a given radius would suggest that the turbulent bulk motions within LMC molecular clouds are more quiescent than in the B08 GMCs. If, on the other hand, GMCs in the LMC manage to achieve rough dynamic equilibrium, then their relatively narrow linewidths would imply that they have lower mass surface densities than the B08 clouds.

To fit the $R - \sigma_v$ relationship for the MAGMA data, we used the BCES bisector linear regression method presented by Akritas & Bershady (1996), which is designed to take measurement errors in both the dependent and independent variable, and the intrinsic scatter of a dataset into account.⁵ For our analysis of all the Larson relations, we use the bisector method because our goal is to estimate the intrinsic relation between the cloud properties (e.g. Babu & Feigelson 1996). The best-fitting relation for all 125 clouds in the MAGMA cloud list, illustrated with grey shading in Fig. 4[a], is:

$$\log \sigma_v = (-0.73 \pm 0.08) + (0.74 \pm 0.05) \log R \text{ (BCES bisector)}. \quad (4)$$

Here, and for all other relations presented in this paper, the errors in the regression coefficients are derived using bootstrapping techniques; for relations determined using a BCES estimator, they are consistent with the standard deviation of the regression coefficients derived according to eqn. 30 in Akritas & Bershady (1996) unless otherwise noted. Although the errors in best-fitting relation that we derive using are small, we caution that the form of the relation depends on the linear regression method (for a discussion of this issue in other astronomical contexts, see e.g. Tremaine et al. 2002; Kelly 2007; Blanc et al. 2009). For comparison with other work, the best-fitting relations determined using the BCES ordinary least squares (henceforth OLS(Y|X)) and BCES orthogonal methods are:

⁵ ‘BCES’ stands for bivariate, correlated errors and intrinsic scatter. Software that implements this method is available from: <http://www.astro.wisc.edu/~mab/archive/stats/stats.html>. For our analysis, we assume that measurement errors are uncorrelated.

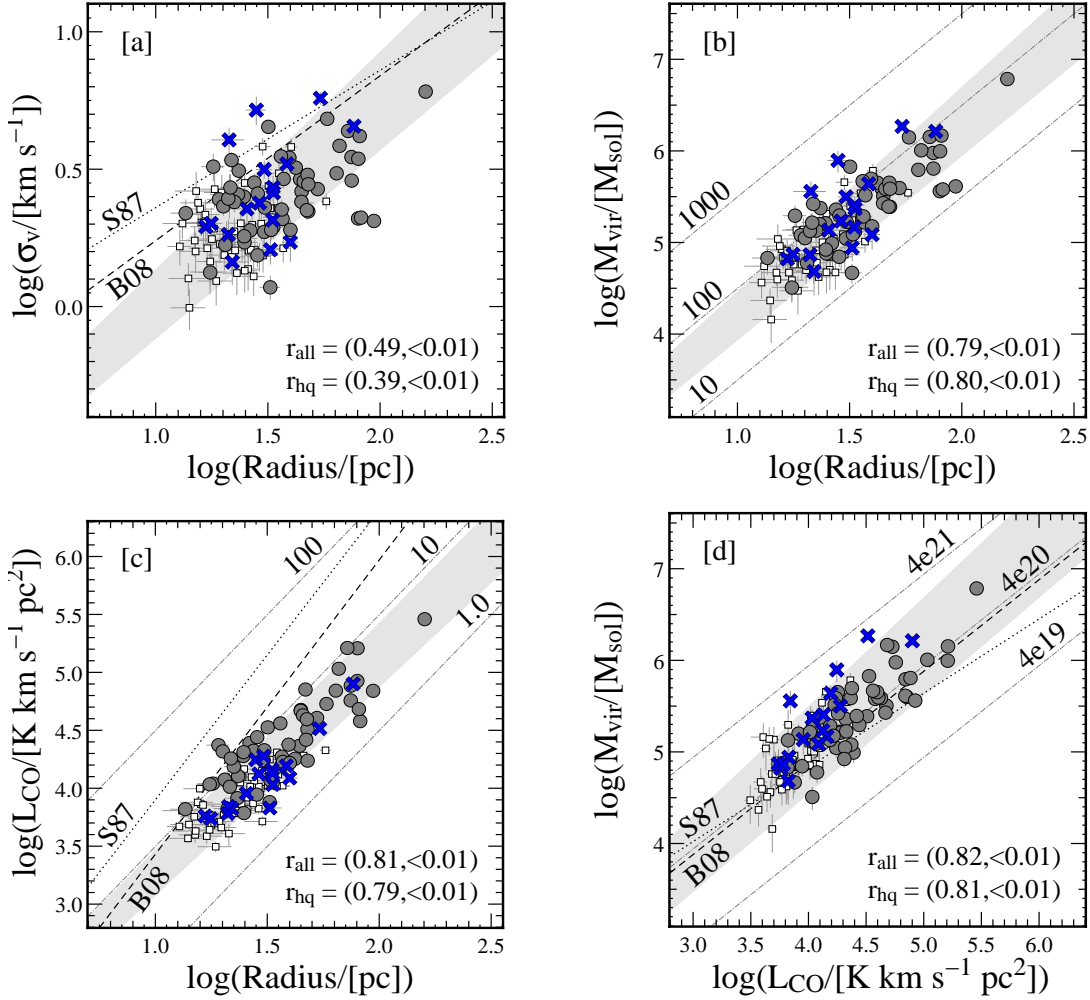


Figure 4. Plots of (a) radius versus velocity dispersion; (b) radius versus virial mass; (c) radius versus CO luminosity; and (d) CO luminosity versus virial mass for the GMCs identified in the MAGMA LMC survey. In each panel, the light grey shaded area represents our BCES bisector fit to the 125 GMCs in the MAGMA cloud list and the $1\text{-}\sigma$ uncertainty in this fit (see text). The black dotted line in each panel shows the standard relation for the S87 inner Milky Way data, while the black dashed line represents the relation determined for extragalactic GMCs by B08. The dot-dashed grey lines represent constant values of CO surface brightness ($I_{\text{CO}} = 1, 10, 100 \text{ K km s}^{-1}$, panel [b]); mass surface density ($\Sigma_{\text{H}_2} = 10, 100, 1000 \text{ M}_\odot \text{ pc}^{-2}$, panel [c]); and CO-to- H_2 conversion factor ($X_{\text{CO}} = 0.4, 4.0, 40 \times 10^{20} \text{ cm}^{-2} (\text{K km s}^{-1})^{-1}$, panel [d]). GMCs belonging to the complete MAGMA LMC cloud list are represented by small open squares, and GMCs in the high quality subsample are indicated using filled grey circles. The blue cross symbols represent GMCs without signs of active star formation. For comparison with the correlations presented in Fig. 5 to 8, Spearman’s rank correlation coefficient and corresponding p -value for all clouds and the high quality subsample are indicated at the bottom right of each panel.

$$\log \sigma_v = (-0.24 \pm 0.09) + (0.40 \pm 0.06) \log R \text{ (BCES OLS}(Y-X)) \quad (5)$$

$$\log \sigma_v = (-0.46 \pm 0.12) + (0.56 \pm 0.08) \log R \text{ (BCES orthogonal)}. \quad (6)$$

The best-fitting relation derived using the FITEXY estimator (Press et al. 1992) is:

$$\log \sigma_v = (-0.37 \pm 0.17) + (0.50 \pm 0.11) \log R \text{ (FITEXY)}. \quad (7)$$

The intrinsic scatter of the MAGMA GMCs around the best-fitting $R - \sigma_v$ relation is greater than the measurement errors in R and σ_v across the observed range of cloud radii. The C_0 values of individual MAGMA GMCs vary between 0.21 and 0.98 $\text{km s}^{-1} \text{ pc}^{-0.5}$. Although LMC clouds may be said to follow the same $R - \sigma_v$ relation as other extragalactic GMCs in the sense that the slope and amplitude of the derived best-fitting relations are similar, their molecular mass surface density is not strictly constant, but instead varies between 15 and 320 $\text{M}_\odot \text{ pc}^{-2}$ (see Fig. 4[b]). An outstanding question, which we investigate further in Section 6, is whether the variation in Σ_{H_2} is stochastic or whether it is related to changes in the environment of the GMCs.

5.2 The size-luminosity relation

Fig. 4[c] presents a plot of CO luminosity versus radius for GMCs in the MAGMA cloud list. Although the $L_{\text{CO}} - R$ relation determined for extragalactic clouds by B08 ($L_{\text{CO}} \approx 7.8_{-3.7}^{+6.9} R^{2.54 \pm 0.20}$) overlaps with the smaller MAGMA clouds, the slope of the $L_{\text{CO}} - R$ relation in the LMC is clearly shallower, such that the CO emission in large LMC molecular clouds is up to an order of magnitude fainter than for GMCs in nearby galaxies. A BCES bisector fit yields:

$$\log L_{\text{CO}} = (1.39 \pm 0.12) + (1.88 \pm 0.08) \log R, \quad (8)$$

for the $L_{\text{CO}} - R$ relation. The relations determined using the BCES OLS(Y|X), BCES orthogonal and FITEXY methods are also shallower than the B08 fit, with slopes of 1.67 ± 0.09 , 2.02 ± 0.10 and 2.17 ± 0.29 respectively.

The median CO surface brightness of GMCs in the MAGMA cloud list is 4.8 K km s^{-1} , and the median absolute deviation of the GMCs around this value is ~ 30 per cent. This corresponds to an average mass surface density of only $\langle \Sigma_{\text{H}_2} \rangle \sim 20 \text{ M}_{\odot} \text{ pc}^{-2}$ for the MAGMA clouds if we adopt the Galactic X_{CO} value ($2 \times 10^{20} \text{ cm}^{-2} (\text{K km s}^{-1})^{-1}$, e.g. Strong & Mattox 1996) and $\langle \Sigma_{\text{H}_2} \rangle \sim 50 \text{ M}_{\odot} \text{ pc}^{-2}$ if we use the median X_{CO} value of the MAGMA cloud list ($X_{\text{CO}} = 4.7 \times 10^{20} \text{ cm}^{-2} (\text{K km s}^{-1})^{-1}$, see Table 1). Individual GMCs have I_{CO} values between 1.8 and 20.4 K km s^{-1} . Some of the variation in I_{CO} appears to be related to the location of the GMCs: for clouds that are coincident with the stellar bar (defined as regions where $\Sigma_{*} > 100 \text{ M}_{\odot} \text{ pc}^{-2}$, see Fig. 1), the median CO surface brightness is 9.1 K km s^{-1} . We examine the relationship between the CO emission in LMC molecular clouds and the stellar mass surface density more closely in Section 6.2.1.

5.3 The calibration between virial mass and CO luminosity

Fig. 4[d] presents a plot of the virial mass estimate versus the CO luminosity for the MAGMA clouds. The LMC clouds appear to be in reasonable agreement with the slope of the relation determined for the B08 extragalactic GMC data ($M_{\text{vir}} \approx 7.6_{-2.6}^{+3.2} L_{\text{CO}}^{1.00 \pm 0.04}$), although offset slightly to higher M_{vir} values. A BCES bisector fit to the $M_{\text{vir}} - L_{\text{CO}}$ relation for the complete MAGMA LMC cloud list yields:

$$\log M_{\text{vir}} = (0.50 \pm 0.25) + (1.13 \pm 0.06) \log L_{\text{CO}}. \quad (9)$$

The slopes of the relations determined using the BCES OLS(Y|X), BCES orthogonal and FITEXY methods are 0.99 ± 0.06 , 1.16 ± 0.07 and 0.97 ± 0.17 respectively. Even for the steepest BCES fit, the systematic variation in X_{CO} with mass is small, corresponding to only a factor of two increase in X_{CO} for GMC masses between 3×10^4 and $3 \times 10^6 \text{ M}_{\odot}$. The rms scatter of the MAGMA GMCs around the best-fitting relation corresponds to a similar variation in X_{CO} .

The median value of X_{CO} for the MAGMA LMC clouds is $4.7 \times 10^{20} \text{ cm}^{-2} (\text{K km s}^{-1})^{-1}$. This is in excellent agreement with the values derived by B08 and Blitz et al. (2007) for their extragalactic GMCs, and the LMC value obtained by the SEST Large Programme (Israel et al. 2003), but lower than the value derived from the NANTEN LMC survey ($7 \times 10^{20} \text{ cm}^{-2} (\text{K km s}^{-1})^{-1}$, Fukui et al. 2008). While the CPROPS cloud decomposition algorithm aims to minimize instrumental effects, part of this discrepancy may be due to the difference in angular resolution between the two surveys. GMCs are constituted by dense ($n \approx 10^3 \text{ cm}^{-3}$) CO-bright peaks embedded in more diffuse gas with lower CO brightness; as noted by several previous authors (e.g. Pineda et al. 2009; Bolatto et al. 2003), observations with coarser resolution trace larger physical structures and hence derive larger values for X_{CO} . In principle, the discrepancy could also arise from MAGMA's observational strategy, which excluded clouds in the NANTEN catalogue with low CO surface brightness (recall that $X_{\text{CO}} \equiv \Sigma_{\text{H}_2}/2.2I_{\text{CO}}$). In practice, however, we do not expect that our target selection has a significant impact on the average MAGMA X_{CO} value, since there are only four NANTEN clouds with $L_{\text{CO}} > 7000 \text{ K km s}^{-1} \text{ pc}^2$ and peak $I_{\text{CO}} < 1 \text{ K km s}^{-1}$.

6 GMC PROPERTIES AND INTERSTELLAR CONDITIONS

In this section, we explore the variation of the physical properties of the MAGMA LMC clouds in response to local interstellar conditions. We measure the local H I column density, stellar mass surface density, interstellar radiation field and external pressure for each GMC using the maps described in Section 2.2, taking the mean value of all independent pixels with integrated CO emission greater than 1 K km s^{-1} . We measure the strength of correlations between the GMC and interstellar properties using the Spearman rank correlation coefficient, r , a non-parametric rank statistic that measures the strength of monotone association between two variables. The statistical significance of r is assessed by calculating the corresponding p -value, which is the two-sided significance level of r 's deviation from zero. We consider p -values less than 0.01 to provide statistically significant evidence against the null hypothesis (i.e. that there is no underlying correlation between the variables). We regard $|r|$ values greater than 0.6 as strong correlations (or anti-correlations if $r < 0$), $|r|$ values between 0.4 and 0.6 as moderate correlations, and $|r|$ values between 0.2 and 0.4 as weak correlations. We regard correlations with $|r|$ values less than 0.2 to

Table 2. Results of the correlation tests between the properties of the MAGMA GMCs and properties of the interstellar environment. The properties used in the comparison are listed in columns 1 and 2. The results of the correlation tests for the complete MAGMA cloud list are shown in columns 3 to 5; the results for the 57 high quality GMCs are shown in columns 6 to 8. The results list $\langle r \rangle$, $\langle p \rangle$ and σ_p , where $\langle r \rangle$ is the median Spearman correlation coefficient obtained in the error trials (see text), $\langle p \rangle$ is the median of the corresponding p -values, and σ_p is the standard deviation of the p -values.

Environment	GMC	All GMCs			HQ GMCs		
		$\langle r \rangle$	$\langle P \rangle$	$\sigma(P)$	$\langle r \rangle$	$\langle P \rangle$	$\sigma(P)$
G_0	R	-0.16	0.06	0.03	-0.27	0.03	0.01
	σ_v	-0.03	0.71	0.16	0.13	0.39	0.11
	$\langle T_{\text{pk}} \rangle$	0.18	0.04	0.03	0.26	0.05	0.03
	I_{CO}	0.17	0.06	0.03	0.38	< 0.01	< 0.01
	I_{CO} , SF only	0.13	0.17	0.08	0.38	< 0.01	< 0.01
	Σ_{H_2}	0.06	0.52	0.20	0.27	0.04	0.03
	Σ_{H_2} , SF only	0.17	0.08	0.05	0.37	< 0.01	< 0.01
	X_{CO}	-0.06	0.51	0.21	-0.03	0.83	0.14
Σ_*	R	-0.13	0.13	0.05	-0.10	0.36	0.08
	σ_v	0.00	0.87	0.10	0.09	0.54	0.13
	$\langle T_{\text{pk}} \rangle$	0.34	< 0.01	< 0.01	0.55	< 0.01	< 0.01
	I_{CO}	0.34	< 0.01	< 0.01	0.40	< 0.01	< 0.01
	Σ_{H_2}	0.06	0.44	0.19	0.10	0.41	0.14
	X_{CO}	-0.19	0.04	0.03	-0.22	0.08	0.04
NHI	R	0.12	0.19	0.05	0.28	0.04	0.01
	σ_v	0.30	< 0.01	< 0.01	0.43	< 0.01	< 0.01
	$\langle T_{\text{pk}} \rangle$	-0.07	0.36	0.15	-0.15	0.24	0.10
	I_{CO}	-0.05	0.58	0.14	-0.03	0.90	0.08
	Σ_{H_2}	0.25	< 0.01	< 0.01	0.26	0.06	0.03
	X_{CO}	0.28	< 0.01	< 0.01	0.29	0.03	0.02
	X_{CO} , SF only	0.32	< 0.01	< 0.01	0.28	0.04	0.02
P_h	R	0.03	0.76	0.15	0.19	0.15	0.05
	σ_v	0.32	< 0.01	< 0.01	0.49	< 0.01	< 0.01
	$\langle T_{\text{pk}} \rangle$	0.13	0.16	0.09	0.25	0.07	0.04
	I_{CO}	0.16	0.07	0.03	0.25	0.06	0.03
	Σ_{H_2}	0.27	< 0.01	< 0.01	0.34	0.01	0.01
	X_{CO}	0.14	0.13	0.08	0.14	0.32	0.12

be very weak and therefore unlikely to have practical significance, even if their p -value is small.

Each correlation test was repeated for the complete MAGMA LMC cloud list and for the high quality subsample. Since the Spearman rank correlation test does not account for measurement uncertainties, we performed 500 trials of each correlation test in which we offset each cloud property measurement by a fraction of its uncertainty. As for the KS test in Section 4, the value of a cloud property measurement in each trial was displaced by $k\Delta x$, where Δx is the absolute uncertainty in the cloud property measurement and k is a uniformly distributed random number between -1 and 1. We consider our correlation result to be robust and significant if i) the correlation coefficients obtained in the trials are narrowly distributed around the original (i.e. unperturbed) value of r , ii) the corresponding p -values are narrowly distributed around zero, i.e. $\langle p \rangle \leq 0.01$ and $\sigma_p \leq 0.01$, and iii) $|r| \geq 0.2$ for both the complete MAGMA cloud list and the high quality subsample. The results of all the correlation tests are presented in Table 2. As a reference for the values obtained in these comparisons, we conducted equivalent correlation tests for the Larson scaling relations shown in Fig. 4, and present the results in Table 3. We note that the size-linewidth relation is only a weak to moderate correlation: for all 125 GMCs in the MAGMA cloud list $\langle r \rangle = 0.48$, while for the high quality GMCs $\langle r \rangle = 0.39$. The size-luminosity and mass-luminosity relations are more strongly correlated ($\langle r \rangle \approx 0.8$); this is expected since L_{CO} and M_{vir} are both dependent on R and σ_v .

6.1 Comparison with G_0

In Fig. 5, we plot the radius, velocity dispersion, average peak CO brightness, CO surface brightness, mass surface density and CO-to-H₂ conversion factor of the MAGMA clouds as a function of the local interstellar radiation field, G_0 . All the plots show considerable scatter and none of the correlations satisfy our criteria for significance. Contrary to what might be expected from classic photodissociation models (e.g. van Dishoeck & Black 1988), there is no general trend between the G_0 and X_{CO} ,

Table 3. Results of the correlation tests for Larson’s scaling relations in the LMC. The relation is listed in column 1. The results of the correlation tests for the complete MAGMA cloud list are shown in column 2; the results for the 57 high quality GMCs are shown in column 3. The results are expressed in the form $(\langle r \rangle, \langle p \rangle, \sigma_p)$, where $\langle r \rangle$ is the median Spearman correlation coefficient obtained in the error trials (see text), $\langle p \rangle$ is the median of the corresponding p -values, and σ_p is the standard deviation of the p -values.

Relation	All GMCs			HQ GMCs		
	$\langle r \rangle$	$\langle P \rangle$	$\sigma(P)$	$\langle r \rangle$	$\langle P \rangle$	$\sigma(P)$
$R - \sigma_v$	0.48	< 0.01	< 0.01	0.39	< 0.01	< 0.01
$R - L_{\text{CO}}$	0.80	< 0.01	< 0.01	0.80	< 0.01	< 0.01
$L_{\text{CO}} - M_{\text{vir}}$	0.81	< 0.01	< 0.01	0.80	< 0.01	< 0.01

even for clouds without signs of active star formation (i.e. where G_0 is dominated by the external field). An earlier analysis of the MAGMA data for the molecular ridge region also found that X_{CO} was insensitive to variations in the radiation field strength (Pineda et al. 2009).

6.2 Comparison with the interstellar pressure

In this subsection, we investigate whether the physical properties of the MAGMA clouds vary with the interstellar pressure. We estimate the total pressure at the molecular cloud boundary using the expression given by E89 for a two-component disc of gas and stars in hydrostatic equilibrium:

$$P_h = \frac{\pi G}{2} \Sigma_g \left(\Sigma_g + \frac{\sigma_g}{\sigma_*} \Sigma_* \right). \quad (10)$$

In this expression, σ_g and σ_* are the velocity dispersions of the gas and stars respectively, Σ_g is the mass surface density of the gas and Σ_* is the stellar mass surface density. The term in brackets on the right hand side of Equation 10 is an estimate for the total dynamical mass within the disc gas layer. We assume a constant velocity dispersion of $\sigma_g = 9 \text{ km s}^{-1}$ for the gas, based on the average dispersion of the H I line profiles across the LMC (see also Wong et al. 2009), and $\sigma_* = 20 \text{ km s}^{-1}$ for the stars (van der Marel et al. 2002). For Σ_* , we use the stellar mass surface density map of Yang et al. (2007) described above, and we estimate $\Sigma_g \equiv \Sigma_{\text{HI}}[\text{M}_\odot \text{ pc}^{-2}] = 1.089 \times 10^{-20} N(\text{HI})[\text{cm}^{-2}]$ directly from the H I column density map (the conversion between $N(\text{HI})$ and Σ_g includes a factor of 1.36 by mass for the presence of helium). We note that the H I and stars make similar contributions to the total mass surface density at the locations of GMCs in the LMC: $\langle \Sigma_* \rangle = 48 \text{ M}_\odot \text{ pc}^{-2}$, and $\langle \Sigma_g \rangle = 30 \text{ M}_\odot \text{ pc}^{-2}$; for comparison, E89 adopted $\langle \Sigma_* \rangle = 55 \text{ M}_\odot \text{ pc}^{-2}$ and $\langle \Sigma_g \rangle = 12 \text{ M}_\odot \text{ pc}^{-2}$ as characteristic values in the Milky Way disc.

Along sightlines to GMCs, our definition of P_h provides an estimate of the pressure at the surface of the molecular cloud rather than at the disc midplane, since the weight of a GMC is likely to make a significant contribution to the total midplane pressure. Further caveats are (i) the assumption that the disc is supported against gravity solely by the observed velocity dispersions, and (ii) that the interaction between the LMC and the Galactic halo may make a significant contribution to the pressure that is not accounted for by our simple estimate in Equation 10. In the following, we first compare the cloud properties to two independent components of P_h for which we have an empirical tracer: i) the stellar mass surface density, Σ_* and ii) the atomic gas surface density, Σ_g .

6.2.1 Comparison with Σ_*

In Fig. 6, we plot the properties of the MAGMA clouds versus Σ_* . The correlation tests indicate weak but significant correlations between Σ_* and $\langle T_{\text{pk}} \rangle$ (panel [c]) and I_{CO} (panel [d]); these correlations are strengthened if we restrict our analysis to high quality GMCs. The existence of these trends suggests that the GMCs in the LMC do respond to the presence of the galaxy’s stellar population, despite evidence that the stellar bar may be physically offset from the gas disc (e.g. Zhao & Evans 2000; Nikolaev et al. 2004).

6.2.2 Comparison with Σ_g

In Fig. 7, we plot the cloud properties as a function of the atomic gas surface density, Σ_g , which is estimated from the total H I column density along the line-of-sight. We find a weak but robust correlation between Σ_g and σ_v (panel [b]); again, the correlation is stronger if only high quality GMCs are considered. There is some indication that Σ_{H_2} (panel [e]) and X_{CO} (panel [f]) also increase with the H I column density – as would be expected if σ_v increases without a corresponding increase in

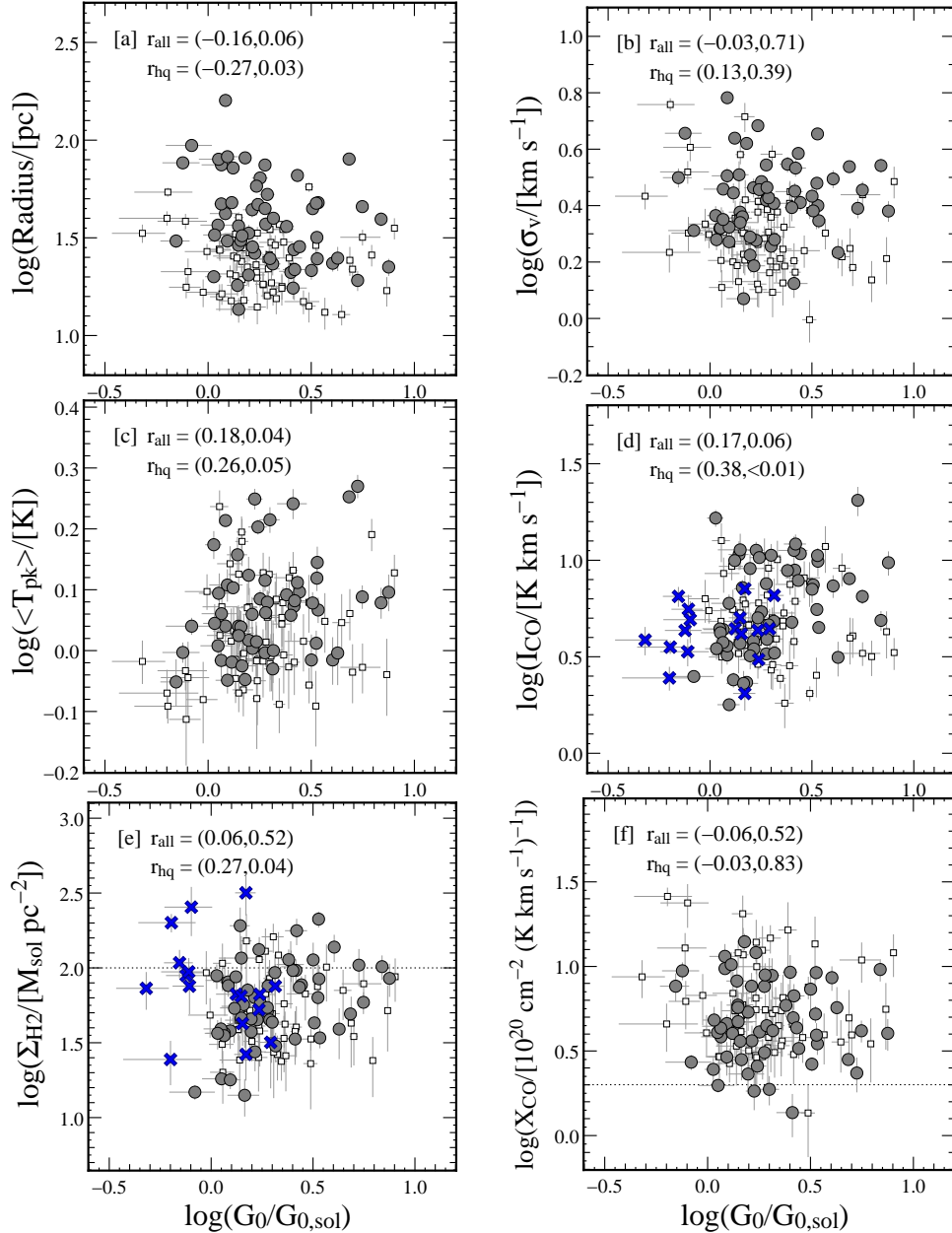


Figure 5. Properties of the MAGMA GMCs, plotted as a function of the local interstellar radiation field, $G_0/G_{0,\odot}$: (a) radius; (b) velocity dispersion; (c) average peak CO temperature; (d) CO surface brightness, I_{CO} ; (e) molecular mass surface density, Σ_{H_2} ; and (f) CO-to- H_2 conversion factor, X_{CO} . The plot symbols are the same as in Fig. 4. The horizontal dotted lines in panels [e] and [f] indicate $\Sigma_{\text{H}_2} = 100 M_{\odot} \text{pc}^{-2}$ and $X_{\text{CO}} \sim 2 \times 10^{20} \text{cm}^{-2} (\text{K km s}^{-1})^{-1}$, i.e. values that apply to GMCs in the inner Milky Way. The Spearman rank correlation coefficient and corresponding p -value for the complete MAGMA cloud list and high quality subsample are indicated at the top left of each panel.

cloud size or CO luminosity – but the correlations are not significant if only high quality GMCs are considered. An important caveat for interpreting Fig. 7 is that H I line profiles in the LMC are notoriously complex, exhibiting two well-defined velocity components in some parts of the LMC’s disc (especially in the south-east, e.g. Luks & Rohlfs 1992). The CO emission is almost invariably associated with only one H I velocity component (Wong et al. 2009), so the H I column density that is physically associated with a GMC is almost certainly overestimated by the total $N(\text{H I})$ along the line-of-sight in these regions. Excluding GMCs located in the south-east of the LMC (i.e. clouds with right ascension above 05h38m and declination below -68d30m (J2000)) from our comparisons between the cloud properties and Σ_g suggests that the correlations between Σ_g and σ_v is not severely contaminated by the contribution of the secondary H I velocity component to $N(\text{H I})$.

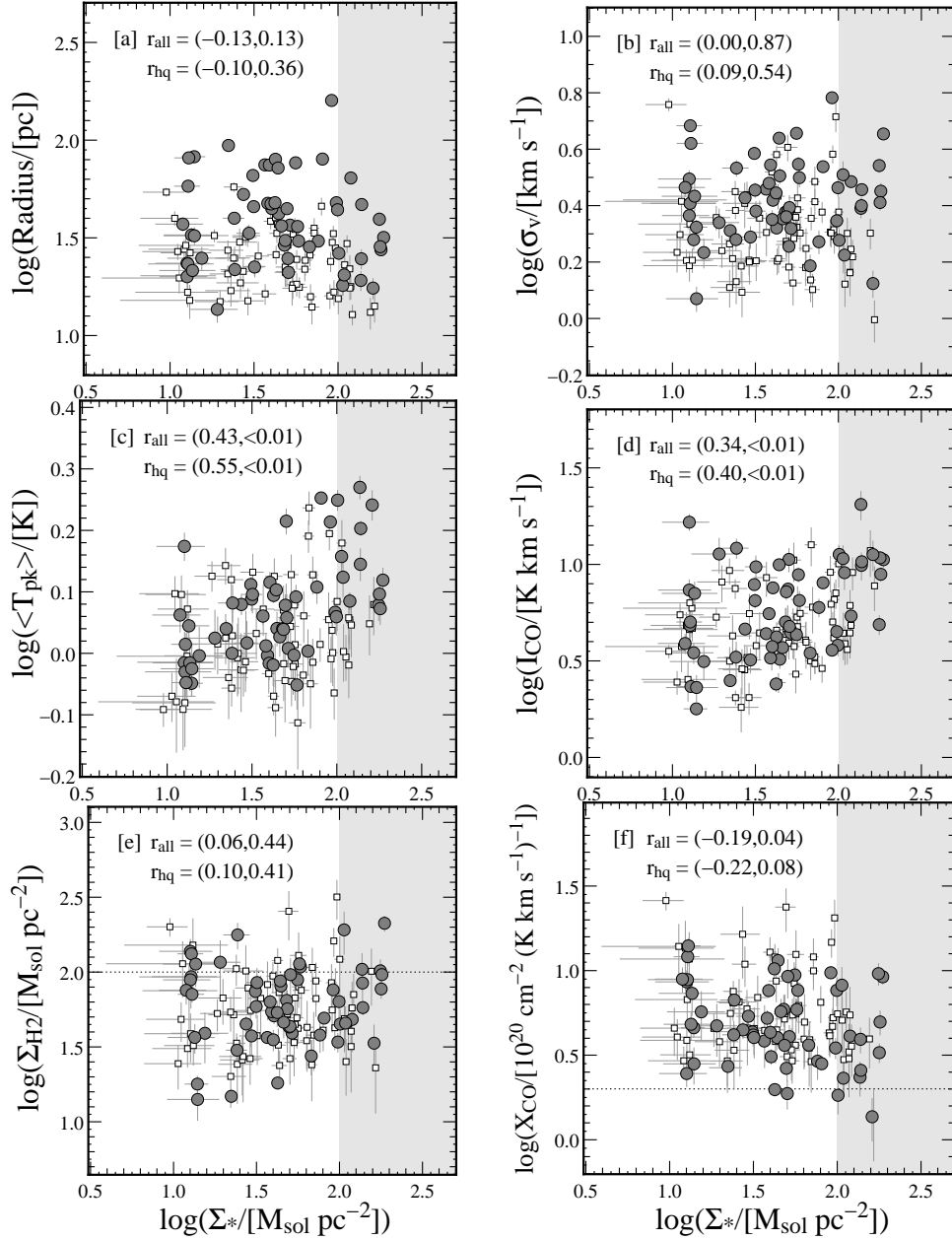


Figure 6. Properties of the MAGMA clouds, plotted as a function of the stellar mass surface density, Σ_* . The panels, plot symbols and annotations are the same as in Fig. 5. The grey shading indicates regions where $\Sigma_* \geq 100 M_{\odot} \text{pc}^{-2}$, corresponding to the stellar bar region denoted by the ellipse in Fig. 1.

6.2.3 Comparison with P_h

The comparison between properties of the MAGMA clouds and Σ_g is helpful for interpreting the plots in Fig. 8. In particular, both σ_v and Σ_{H_2} increase in regions with higher P_h , following their behaviour in regions with high H I column density. The dominant physics underlying these correlations may therefore be the importance of an atomic shielding layer for the survival of H_2 molecules, rather than pressure regulation. Σ_{H_2} and P_h is more strongly correlated with P_h than with Σ_g however, and we observe that there are few clouds with low I_{CO} or Σ_{H_2} in regions with high Σ_* (panels [d] and [e] of Fig. 6). Insofar as I_{CO} and Σ_{H_2} are reliable tracers of the H_2 surface density, this provides some indication that shielding alone may not regulate the H_2 surface density in regions of the LMC where the interstellar gas pressure is high.

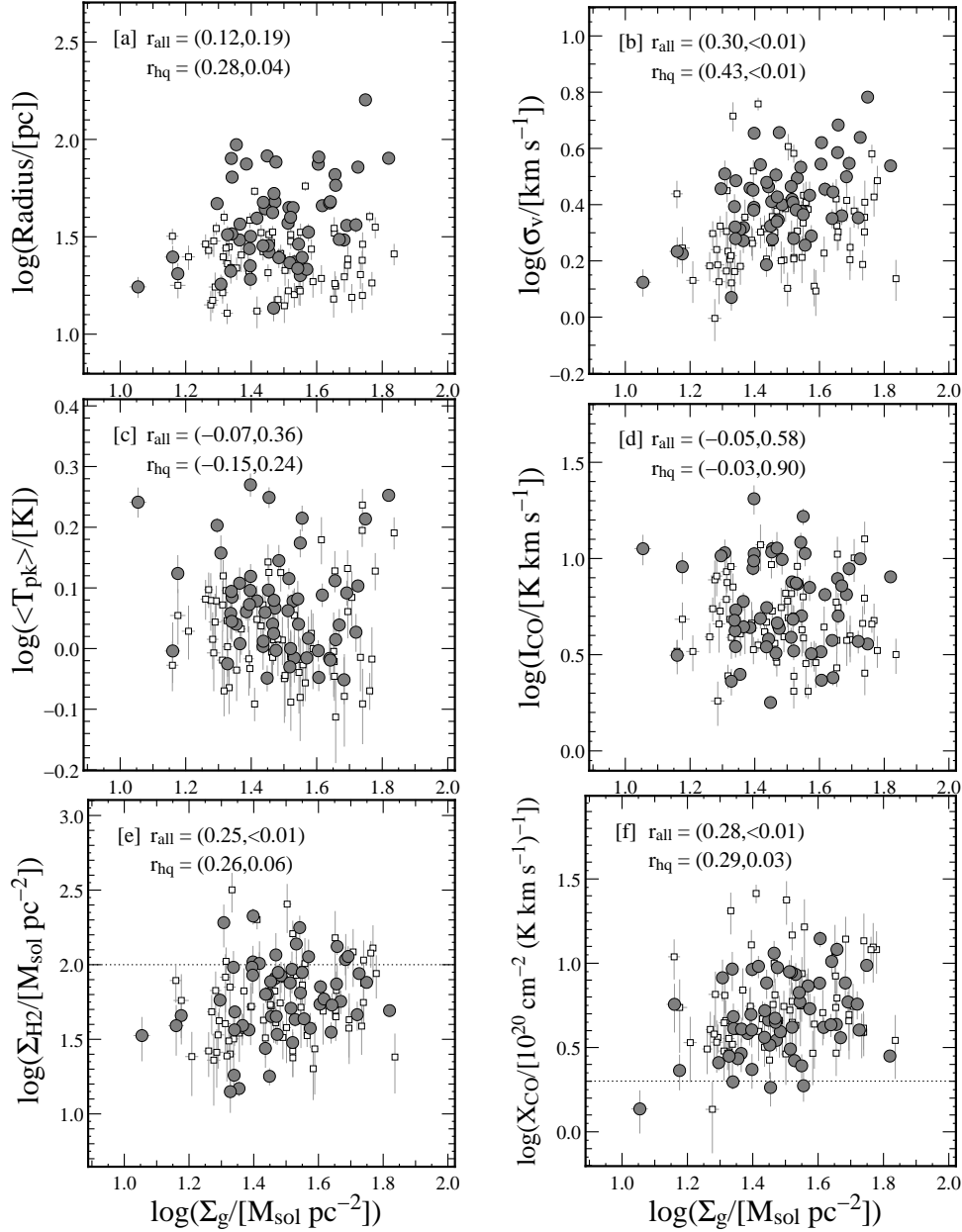


Figure 7. Properties of the MAGMA clouds, plotted as a function of the atomic gas surface density, Σ_g . The panels, plot symbols and annotations are the same as in Fig. 5.

7 DISCUSSION

7.1 Properties of young GMCs

In Section 4, we investigated the physical properties of the young GMC candidates in the MAGMA LMC cloud list, finding that sightlines through these clouds tend to have lower T_{\max} and $\langle T_{\text{pk}} \rangle$ than sightlines through star-forming GMCs of equivalent size. Models of the $^{12}\text{CO}(J = 1 \rightarrow 0)$ emission from GMCs indicate that the emission arises from a large number of optically thick clumps that are not self-shadowing (e.g. Wolfire et al. 1993). For each independent sightline through a GMC, the observed peak CO brightness is then a measure of the total projected area of the optically thick clumps within the beam area, weighted by their brightness temperature, which should correspond to the kinetic temperature of the CO-emitting gas if emission in the clumps is optically thick (e.g. Maloney & Black 1988). The usual assumption is that the distribution of clump sizes and the brightness temperature do not vary significantly between sightlines, and that the observed CO brightness measures the number of clumps – and hence the total amount of molecular gas – within the telescope beam. While this assumption may be justified for clouds in the inner disc of the Milky Way (S87), it is worth noting that the peak CO brightness results

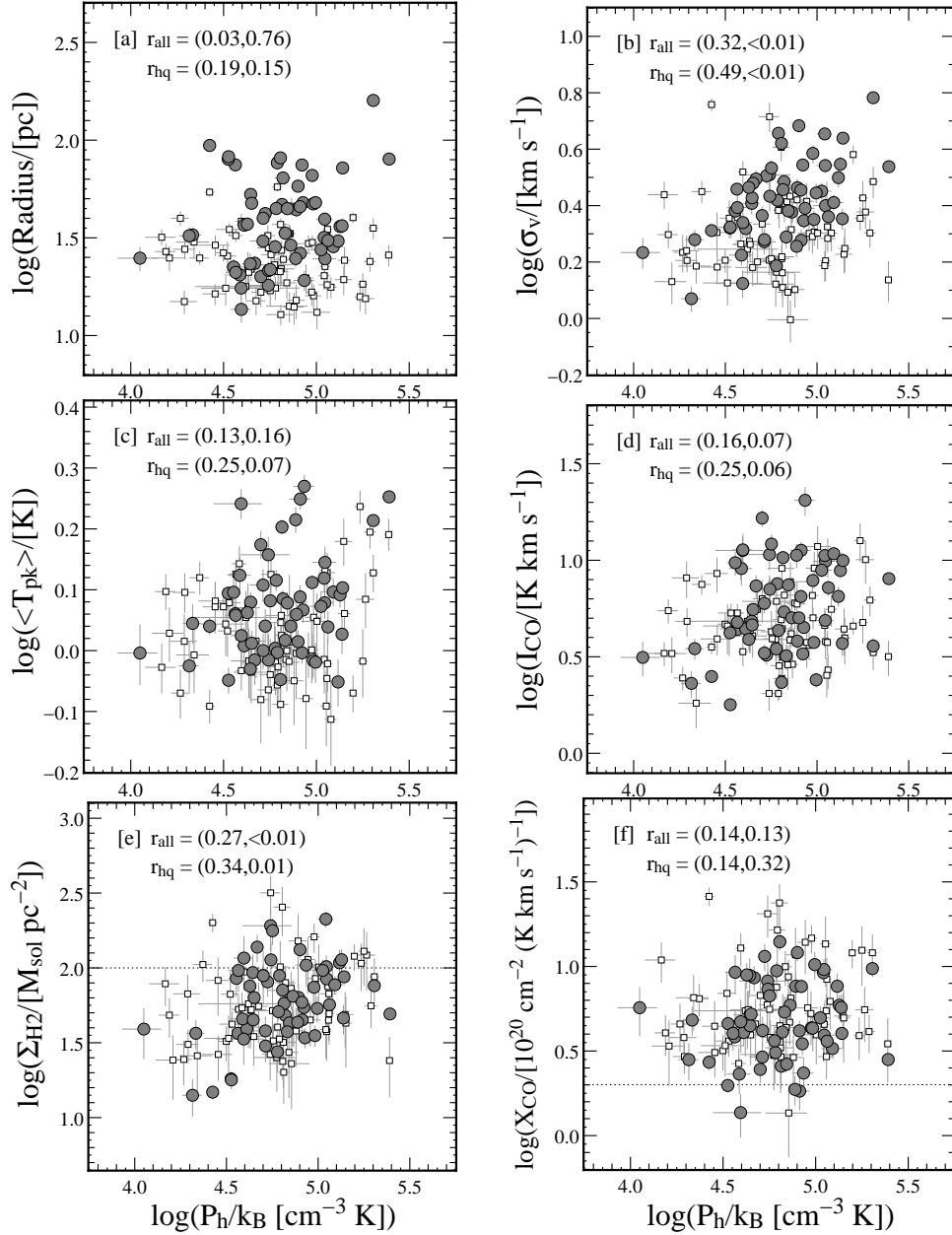


Figure 8. Properties of the MAGMA clouds, plotted as a function of the interstellar pressure, P_h . The panels, plot symbols and annotations are the same as in Fig. 5.

from a combination of the brightness temperature, the number of CO-emitting clumps within the beam, and their average size. A possible interpretation for the different average peak CO brightness of star-forming and non-star-forming GMCs is that there are fewer CO-emitting clumps in GMCs without star formation, leading to a lower angular filling factor of CO emission. Alternatively, colder gas temperatures in the dormant CO-emitting substructures within non-star-forming GMCs could lead to a lower average brightness temperature for the clump ensemble.

As our young GMC candidates tend to have a lower $\langle T_{\text{pk}} \rangle$ and T_{max} values than star-forming GMCs of comparable size, it might be expected that their total CO luminosity would also be fainter. However, the KS tests reveal no systematic differences between the distributions of L_{CO} and I_{CO} for the various cloud samples, which suggests that the regions of high CO brightness in the star-forming GMCs are restricted to a relatively small number of pixels in the MAGMA data subcubes. This is consistent with the view of star formation as a highly localised process: occupying only a small fraction of the total cloud volume, star-forming clumps have temperatures and densities that are much higher than in the bulk of the GMC, most of which does not participate directly in star formation. The lower $\langle T_{\text{pk}} \rangle$ and T_{max} of non-star-forming GMCs would seem

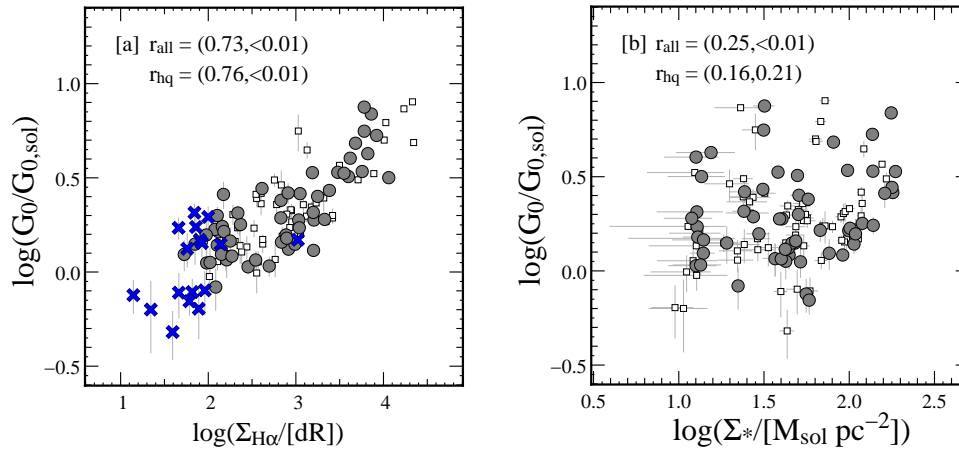


Figure 9. The radiation field at the location of the MAGMA clouds, plotted as a function of (a) the H α surface brightness, as observed by SHASSA (Gaustad et al. 2001), and (b) the stellar mass surface density. Plot symbols are the same as in Fig. 4. The Spearman correlation coefficient and corresponding p -value for all 125 MAGMA GMCs and the high quality subsample are indicated at the top left of each panel.

to provide some preliminary evidence that the general characteristics of substructure within non-star-forming GMCs in the Milky Way – i.e. cooler clumps that are less massive and more diffuse than in star-forming GMCs (e.g. Williams et al. 1994; Williams & Blitz 1998) – will also be found to apply in the LMC.

Finally, we found a clear trend for the young GMC candidates to be located in regions where G_0 is relatively weak. A straightforward explanation for this result is that once young massive stars begin to form, they are an important source of dust-heating within LMC molecular clouds. Importantly, this would mean that G_0 is not strictly tracing the ambient (i.e. external) radiation field incident on a GMC, but instead contains a significant contribution from the massive stars that are within – or have recently emerged from – their GMC progenitor. A strong correlation between G_0 and H α surface brightness for all the MAGMA LMC clouds (see Fig. 9) indicates a strong connection between dust heating and star-formation activity, which would seem to support this interpretation.

7.2 The origin of Larson’s laws

Despite the longevity of Larson’s scaling relations, a complete theoretical explanation for the origin of the size-linewidth relation is still lacking. Considerable effort has been devoted to demonstrating that the observed size-linewidth relationship can be reproduced by realistic models of interstellar turbulence (e.g. Mac Low & Klessen 2004; Ballesteros-Paredes et al. 2007, and references therein), and that turbulence in the cold gas phase is both universal and nearly invariant (e.g. Heyer & Brunt 2004), but differences between the working variables and descriptive tools available to theory and observation represent a significant obstacle to making turbulent models empirically falsifiable. In many instances, however, older explanations for the origin of Larson’s laws have not been thoroughly tested, since there are few extragalactic datasets that are comparable to the Milky Way molecular cloud samples that guided the development of these early models. In this section, we therefore consider whether the MAGMA data are consistent with two analytic models for the origin of Larson’s laws: the photoionization-regulated star formation theory proposed by M89 and the model of molecular clouds as virialized polytropes proposed by E89.

7.2.1 Comparison with McKee (1989)

The photoionization-regulated theory of star formation proposed by M89 provides one possible explanation for the origin of Larson’s laws. In this theory, molecular clouds evolve towards an equilibrium state where energy injection from newborn low-mass stars halts the clouds’ gravitational contraction. Equilibrium depends on the level of photoionization by the interstellar far-ultraviolet (FUV) radiation field because ambipolar diffusion governs the rate of low-mass star formation in the cloud; in turn, the rate of ambipolar diffusion is regulated by the ionization fraction, which depends on the interstellar FUV radiation field in the bulk of the molecular cloud. A second factor that determines the equilibrium state of the GMCs is the local dust abundance, since dust shields H $_2$ molecules against photodissociation. Notably, the M89 theory predicts that molecular clouds in equilibrium should have uniform extinction, rather than constant column density: clouds in environments

with low dust-to-gas ratios and/or strong radiation fields will require larger column densities to attain the equilibrium level of extinction, and should therefore follow a $R - \sigma_v$ relation with a higher coefficient than the Milky Way relation. Recent measurements of the surface densities of extragalactic GMCs contradict this prediction, instead showing that molecular cloud surface densities in low metallicity environments are similar to, or even lower than, the average mass surface density of Milky Way clouds (e.g. B08, Leroy et al. 2007). The median mass surface density of the MAGMA clouds is $\sim 50 M_\odot \text{pc}^{-2}$, in line with these results.

It is worth noting, however, that low mass surface densities (i.e. less than $\sim 100 M_\odot \text{pc}^{-2}$ for GMCs in sub-solar metallicity environments) are not necessarily inconsistent with the M89 model: the complete prediction by M89 is that the velocity dispersion of molecular clouds should increase as the dust-to-gas ratio decreases, provided that the densities of the CO-emitting clumps within GMCs are comparable to the densities of the clumps in Galactic molecular clouds, and that appropriate corrections for the angular filling fraction of the CO-emitting clumps, \mathcal{C} , have been applied. If the CO-emitting clumps within GMCs have $\mathcal{C} \sim 1$, densities of $n_{\text{H}} = 10^3 \text{ cm}^{-3}$, and clump-to-cloud extinction ratios of $\bar{A}_c/\bar{A}_v \sim 0.3$ – values that M89 regards as typical for molecular clouds in the inner Milky Way disc – then the photoionization-regulated star formation theory predicts that equilibrium is achieved for visual extinctions between $\bar{A}_v \sim 4$ and 8 mag. Equations 5.5 to 5.7 in M89 show that an equilibrium extinction value of $\bar{A}_v \sim 1$ can none the less be obtained in an environment with the LMC’s typical dust-to-gas ratio (~ 0.3 , Dobashi et al. 2008) if the CO-emitting clumps within GMCs have an angular filling fraction of $\mathcal{C} = 0.25$ and a typical density of $n_{\text{H}} = 10^{4.5} \text{ cm}^{-3}$, and if the fraction of the total cloud mass residing in these dense clumps is ~ 45 per cent. While agreement with the M89 model is theoretically possible, it requires the density contrast in GMCs in the LMC to be more extreme than in Milky Way clouds. \mathcal{C} values less than unity have previously been invoked to explain the low T_{pk} measurements for LMC clouds (e.g. Wolfire et al. 1993; Kutner et al. 1997; Garay et al. 2002), but average densities of $n_{\text{H}} \sim 10^{4.5} \text{ cm}^{-3}$ for the CO-emitting clumps seem less plausible. Excitation analyses of millimetre and submillimetre spectral line observations (e.g. Heikkilä et al. 1999; Pineda et al. 2008; Minamidani et al. 2008) have reported clump densities between 10^4 and 10^6 cm^{-3} , but as these studies targeted the LMC’s brightest star-forming regions it remains uncertain whether similar clump densities would be common in molecular clouds throughout the LMC.

A further problem for the photoionization-regulated star formation theory is that there is no sign of a correlation between G_0 and Σ_{H_2} or I_{CO} for GMCs without signs of star formation (blue crosses in panels [d] and [e] of Fig. 5). In the scenario postulated by M89, equilibrium is only achieved prior to the onset of massive star formation: after this, young massive stars rapidly disrupt their natal clouds, destroying the relationship between the gas column density, dust abundance and ambient radiation field. The GMCs that are designated as star-forming in the MAGMA sample contain at least one O star (Kawamura et al. 2009) and their young stellar content makes a significant contribution to the radiation field within the cloud (see Table 1). For GMCs without star formation, however, Σ_{H_2} and I_{CO} should show a correlation with G_0 if their column density is regulated by the ambient radiation field, assuming that the dust-to-gas ratio is roughly constant in the environments of non-star-forming GMCs across the LMC. No such correlation is apparent in panel [d] or [e] of Fig. 5.

Finally, we note that a correlation between the internally-generated radiation field and the H_2 mass surface density would be expected if the star formation efficiency of molecular gas were constant (Leroy et al. 2008), since GMCs with higher H_2 column densities – and presumably higher volume densities – should have a higher surface density of star formation. The correlation tests in Section 6 indicated that Σ_{H_2} for star-forming GMCs in the high quality subsample are associated with higher values of G_0 , but the trend is not significant if we consider all the GMCs in the MAGMA cloud list, or if we use I_{CO} rather than Σ_{H_2} to trace the H_2 mass surface density.

7.2.2 Comparison with Elmegreen (1989)

Another explanation for the origin of Larson’s laws was put forward by E89, who proposed that molecular clouds and their atomic envelopes are virialized, magnetic polytropes (i.e. with internal pressure P that varies with the density ρ according to $P = K\rho^n$, where K is a constant and n is the polytropic index) and with external pressure that is determined by the kinetic pressure of the interstellar medium. In this theory, the radius and density of a molecular cloud complex adjust so that the pressure at the boundary of the atomic envelope equals the ambient kinetic pressure. In this case, molecular clouds within a galaxy have a similar mass surface density because the ambient pressure throughout the galaxy is also roughly uniform. While the notion that molecular clouds can achieve dynamical equilibrium within their lifetime has been disputed (e.g. Hartmann et al. 2001), recent work has highlighted the potential importance of pressure for the formation of molecular gas (e.g. Wong & Blitz 2002; Blitz & Rosolowsky 2004, 2006).

The molecular cloud model proposed by E89 predicts that C_0 and Σ_{H_2} should scale with the total mass of the atomic+molecular

Table 4. A summary of the model parameters which are substituted into Equation 12 in order to produce the plots in Fig. 10. The first column describes the metallicity: either a shallow radial gradient of $-0.05 \text{ dex kpc}^{-1}$ (e.g. Cole et al. 2004), or a constant $Z/Z_{\odot} = 0.5$ for all clouds in assumed. We adopt 05h19m30s -68d53m (J2000) for the location of the LMC’s kinematic centre, and $i = 35^{\circ}$ for the LMC’s inclination (Wong et al. 2009). The second column lists k , the factor by which the measured value of $G_0/G_{0,\odot}$ has been reduced for star-forming clouds in the MAGMA cloud list. We introduce k to account for the fact the radiation field in Equation 12 is the external field incident on the molecular cloud, i.e. it does not include the contribution from young massive stars within the cloud. The third column describes the relationship between the total atomic+molecular mass, M_t , and the molecular mass, $M_m \equiv M_{\text{vir}}$, that we adopt for the clouds. For M1 to M4, we use the mass dependence adopted by E89. The mass dependencies for M5 and M6 are constructed such that the total mass of the cloud complex increases more rapidly than the molecular mass; the coefficient of the mass dependence for these models is then chosen such that $M_t \geq M_m$ for the observed range of MAGMA GMC masses.

Model Identifier	Z/Z_{\odot}	k	Mass Dependency
M1	0.5	1.0	$M_t = 2M_m$
M2	0.5	2.0	$M_t = 2M_m$
M3	Gradient	1.0	$M_t = 2M_m$
M4	Gradient	2.0	$M_t = 2M_m$
M5	Gradient	1.0	$M_t/[M_{\odot}] = (M_m/21.45 M_{\odot})^{1.5}$
M6	Gradient	1.0	$M_t/[M_{\odot}] = (M_m/141.42 M_{\odot})^{2.0}$

cloud complex, due to the increasing weight of the atomic gas layer surrounding large molecular clouds. In Sections 5.1 and 6, we saw that the scatter in the Larson-type scaling relations for the MAGMA clouds implies order of magnitude variations in C_0 and Σ_{H_2} , and also evidence for a weak correlation between Σ_{H_2} and the interstellar pressure (Fig. 8[e]). These trends motivate us to examine more closely whether the MAGMA clouds are consistent with the E89 theory for the origin of Larson’s Laws, once variations in the local radiation field, metallicity and mass of atomic gas surrounding the GMCs are taken into account.

In lieu of Larson’s third law, E89 predicts that the total (i.e. atomic+molecular) mass surface density of molecular cloud complexes will vary according to

$$\frac{M_t}{R_t^2} \approx 190 \pm 90 \left(\frac{P_e}{10^4 \text{ k}_B \text{ cm}^{-3} \text{ K}} \right)^{1/2} M_{\odot} \text{ pc}^{-2}, \quad (11)$$

where P_e is the external pressure on a molecular+atomic cloud complex, M_t is the total mass of the atomic+molecular complex and R_t is the radius of the complex. This equation can be written in terms of observed molecular cloud properties:

$$\frac{M_m}{R_m^2} \approx 380 \pm 250 \left(\frac{P_e}{10^4 \text{ k}_B \text{ cm}^{-3} \text{ K}} \right)^{-1/24} \left(\frac{M_t}{10^5 M_{\odot}} \right)^{1/4} \left(\frac{G_0/G_{0,\odot}}{Z/Z_{\odot}} \right)^{1/2} M_{\odot} \text{ pc}^{-2}, \quad (12)$$

where R_m and M_m are the radius and mass of the molecular part of the cloud complex. The range of coefficients in these equations arise from solutions to the virial theorem for plausible values of the adiabatic index and variations in the ratio of the magnetic field pressure to the kinetic pressure (see fig. 3 in E89). To explore the relative importance of the parameters that contribute to the right hand side of Equation 12, we defined six basic models that use different estimates for the total mass, metallicity and external radiation field of the molecular cloud complexes. For all models, P_e is assumed to be the same as the kinetic pressure of the ambient interstellar medium, i.e. $P_e = P_h/(1 + \alpha + \beta)$ where $\alpha \sim 0.4$ and $\beta \sim 0.25$ are the relative contribution by cosmic-rays and the magnetic field to the total pressure, and P_h is estimated according to Equation 10. The model parameters are summarized in Table 4.

In Fig. 10, we plot the observed values of Σ_{H_2} for the MAGMA clouds against the values predicted by Equation 12 for each of the six models. Fig. 10 shows that the measured values for Σ_{H_2} for the MAGMA clouds are significantly lower than predicted by E89, regardless of which model we adopt. The average mass surface density is sensitive to variations in the metallicity and radiation field, but the LMC would need to have $Z \geq Z_{\odot}$ and $G_0 \leq G_{0,\odot}$ for the MAGMA clouds to be consistent with the closest line of equality in Fig. 10 (which corresponds to the lowest value of the coefficient in Equation 12). The models in which the total complex mass increases faster than the molecular mass (M5 and M6) demonstrate a better agreement with the slopes predicted by E89, but these models are not physically realistic since they imply that the mass of the H I envelopes surrounding the MAGMA clouds is almost an order of magnitude greater than the total H I mass of the LMC ($5 \times 10^8 M_{\odot}$, Staveley-Smith et al. 2003). Reducing the coefficient of the mass dependency in these models would lower the total H I envelope mass and also shift the data towards the line of equality in Fig. 12, but it leads to the unphysical solution that $M_t < M_m$ for low mass MAGMA clouds.

The total atomic+molecular mass of the cloud complex is perhaps the most important source of uncertainty in the present comparison, and we are currently undertaking an analysis of the H I and MAGMA CO datasets that should place empirical

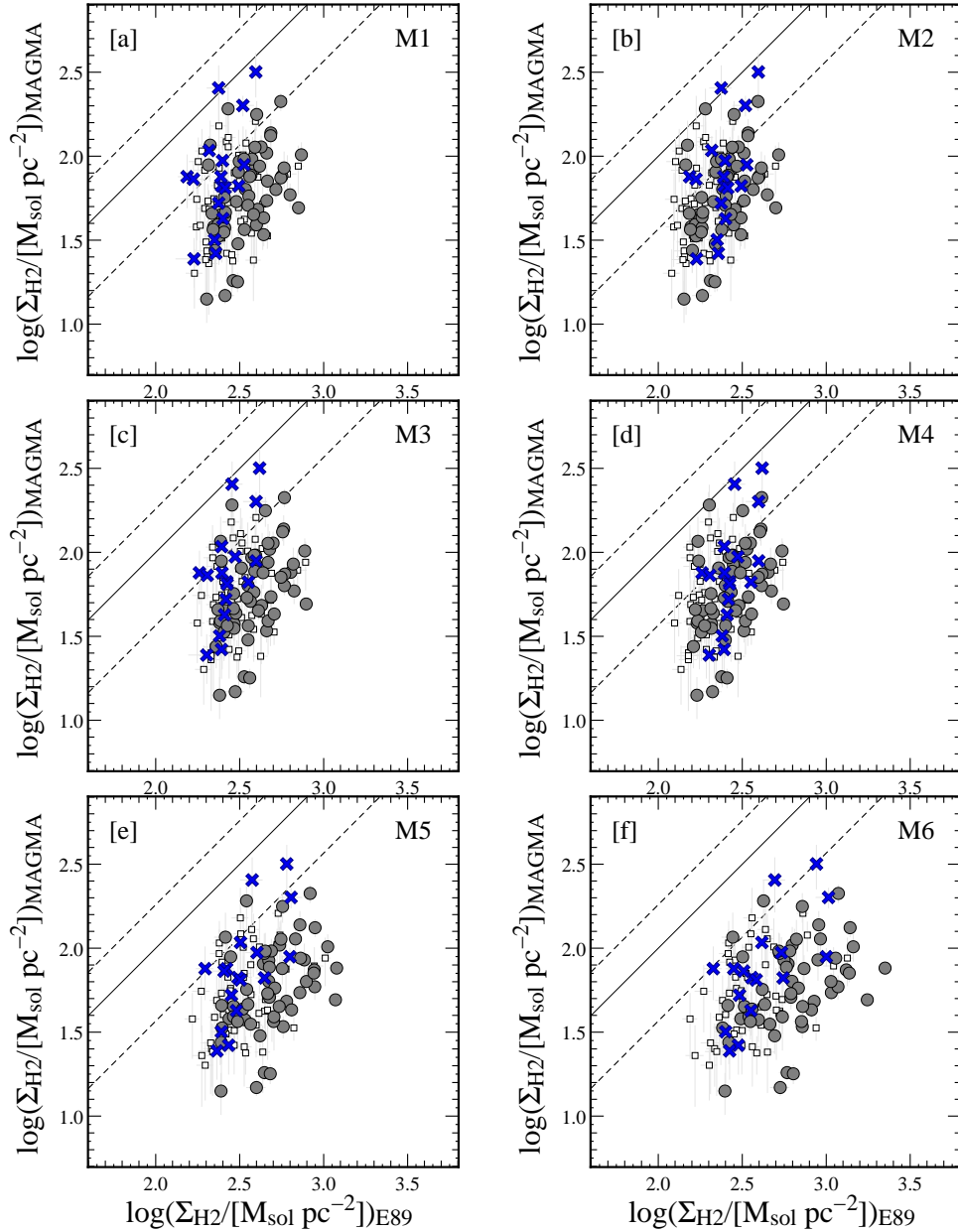


Figure 10. The observed values of Σ_{H_2} for the MAGMA clouds versus the values predicted by E89 for the models of the metallicity, external radiation field and total cloud mass presented in Table 4. Plot symbols are the same as in Fig. 4. The solid line represents equality between the observed and predicted values for the coefficients adopted by E89. The dashed lines indicate the potential shift in the line of equality for the maximum range of the coefficients in Equation 12.

constraints on the mass of the H I gas that is associated with individual MAGMA clouds. However, two further comments regarding the H I data and its potential to constrain the E89 model are worth noting here. First, visual inspection of the CO and H I LMC maps shows that the majority of GMCs are not isolated, but are instead located within a group of molecular clouds that appear to share a common H I envelope. This possibility is not explicitly addressed by E89, but it is important insofar as neighbouring molecular clouds will partially shield each other, reducing the total amount of H I required for the shielding layer. Second, we note that CO emission is detected in regions where the *total* H I column density through the LMC is only $N(\text{HI}) \approx 1 - 2 \times 10^{21} \text{ cm}^{-2}$ (refer fig. 2 of Wong et al. 2009). This is problematic insofar as the H₂ self-shielding theory invoked by E89 requires a uniform shielding layer with $N(\text{HI}) = 1.2 \times 10^{21} \text{ cm}^{-2}$ for a molecular cloud situated in an ambient radiation field $G_0/G_{0,\odot} = 1.5$ and metallicity $Z/Z_{\odot} = 0.5$, assuming an density of $n \approx 60 \text{ H cm}^{-3}$ in the atomic layer (Federman et al. 1979). $N(\text{HI}) = 1.2 \times 10^{21} \text{ cm}^{-2}$ is probably a lower limit: if the gas in the shielding layer is clumpy, then the required column density increases by a factor f/f_{\odot} , where $f = \langle n \rangle^2 / \langle n^2 \rangle$ is the volume filling factor. Part of this discrepancy may be because sightlines towards GMCs in the LMC have significant optical depth: H I absorption studies indicate peak

optical depths between $\tau = 0.4$ and 2.0 near regions with CO emission, implying that the true H I column density is a factor of $\tau/[1 - e(-\tau)] = 1.2 - 2.3$ greater than the observed value (Dickey et al. 1994; Marx-Zimmer et al. 2000). A recent study of the LMC’s far-infrared emission has also proposed a widespread cold atomic gas component with significant optical depth in the LMC in order to explain an excess of emission at $70 \mu\text{m}$ (Bernard et al. 2008).

More generally, we note that plausible variations in the interstellar pressure due to e.g. a widespread ionized gas component or a high rate of cosmic-ray escape would not have a significant impact on the plots in Fig. 10, since the exponent of the pressure term in Equation 12 is small. A significant mass of H₂ without CO emission associated with each GMC would tend to rather magnify than reduce the discrepancy between the MAGMA clouds and the E89 model, moreover, except in a physically improbable scenario where the CO-dark H₂ gas has a greater average density than the CO-emitting region of the GMC. One possible resolution may be the porosity of the LMC’s interstellar medium: as noted above, the calculations in E89 assume a uniform gas layer which provides more effective shielding than gas that is highly clumped. A comparison between the volume filling factor of H I in the solar neighbourhood and in the LMC, plus the inclusion of clumpy cloud structure in the E89 theory, would be required to test this hypothesis however.

7.3 GMC properties: trends with environment

Previous comparative studies of the Milky Way and nearby extragalactic GMC populations have found that GMC properties are relatively uniform, and mostly insensitive to variations in environmental parameters such as the radiation field and dust abundance (e.g. B08, Rosolowsky et al. 2003; Rosolowsky 2007). A possible explanation for this result is that GMCs are strongly bound and hence largely decoupled from conditions in the local ISM. B08 have cautioned, however, that the apparent universality of GMC properties as measured from CO observations may simply reflect the physical conditions required for CO emission to be excited, and that the properties and extent of the H₂ material surrounding a GMC’s high density CO-emitting peaks might indeed be sensitive to local environmental factors, a conclusion that is supported by far-infrared studies of molecular clouds in nearby dwarf galaxies (e.g. Israel 1997; Leroy et al. 2007, 2009). Our analysis tends to support the view that CO-derived properties of GMCs are mostly insensitive to environmental conditions, but there are several exceptions that we discuss below.

7.3.1 GMC properties and Σ_*

In Section 6.2.1, we showed that $\langle T_{\text{pk}} \rangle$ and I_{CO} increase for GMCs located in regions of high Σ_* , without a corresponding variation in R or σ_v . A key variable to explain this result may be the role of the old stars in dust production, as a recent analysis of *Spitzer* mid- and far-infrared data for the LMC indicates that VSGs and polycyclic aromatic hydrocarbon (PAH) molecules are overabundant in the LMC’s stellar bar (Paradis et al. 2009). More specifically, if the abundance of VSGs and/or PAHs were increased by the ejecta from mass-losing old stars, then photoelectric heating of the molecular gas may be more efficient in regions with high Σ_* , potentially raising the CO excitation temperature. Alternatively, a higher overall dust abundance could reduce the selective photodissociation of CO molecules and lead to a higher abundance of CO relative to H₂ for GMCs in the stellar bar. This could occur if H₂ readily self-shields, while the survival of CO molecules relies more on the attenuation of the photodissociating radiation by dust (e.g. Maloney & Black 1988). Although the CO emission from Milky Way molecular clouds is approximately independent of variations in the CO abundance – firstly due to the high optical depth of the ¹²CO($J = 1 \rightarrow 0$) line, and secondly because the angular filling factor of the CO-emitting clumps at any particular radial velocity within the cloud is ~ 1 (see e.g. Wolfire et al. 1993) – this may not be true of LMC molecular clouds (see e.g. Maloney & Black 1988). The low values of T_{pk} for ¹²CO($J = 1 \rightarrow 0$) emission in LMC clouds suggests that the angular filling factor of the CO-emitting clumps is indeed relatively small (see e.g. Kutner et al. 1997; Johansson et al. 1998; Garay et al. 2002), in which case higher CO-to-H₂ ratios might produce higher values of $\langle T_{\text{pk}} \rangle$ and I_{CO} .

Contrary to what might be expected if higher interstellar pressures promote the formation of molecular gas, there is no evidence that R or σ_v for the LMC molecular clouds increases in regions with high Σ_* . The absence of these correlations is perhaps not very significant, however, since our estimate for P_h is dominated by Σ_g for regions with $\Sigma_* \leq 60 \text{ M}_\odot \text{ pc}^{-2}$; if the H I emission along sightlines towards GMCs has significant optical depth, Σ_g will dominate P_h to even higher Σ_* thresholds ($\Sigma_* \sim 100 \text{ M}_\odot \text{ pc}^{-2}$ for $\tau = 1$). A correlation between G_0 and Σ_* might be expected if regions with strong stellar gravity promoted the formation of overdensities within GMCs and enhanced the local star formation rate (e.g. Leroy et al. 2008) or, alternatively, if old stars made a significant contribution to the dust heating. Stronger external heating in the stellar bar region has previously been invoked as an explanation for the higher ¹²CO($J = 2 \rightarrow 1$)/($J = 1 \rightarrow 0$) intensity ratios in inner LMC molecular clouds (Sorai et al. 2001). While the correlation tests in Section 6 provided no clear evidence for a relationship between G_0 and Σ_* , we do not observe clouds with low G_0 values located in regions with $\Sigma_* \geq 100 \text{ M}_\odot \text{ pc}^{-2}$ (see Fig. 9[b]), so

it is possible that enhanced star formation due to strong stellar gravity and/or dust heating by old stars becomes important at higher stellar densities.

7.3.2 GMC properties and $N(\text{H I})$

In Section 6.2.2, we found a weak but significant correlation between $N(\text{H I})$ and σ_v (Fig. 7[b]). Its interpretation is somewhat uncertain, however, since there is no obvious trend between $N(\text{H I})$ and the GMC radius, which would be expected if larger H I column densities were associated with more massive GMCs (assuming that the average density of GMCs also remains constant across the LMC). Some positive association between $N(\text{H I})$ and R would be expected, moreover, simply as a consequence of the size-linewidth relation for LMC molecular clouds. Perhaps the simplest explanation is that the mass and size of GMCs increase with $N(\text{H I})$, but that the GMC radius derived from CO observations is not a sensitive tracer of the true cloud size. Another possibility is that the density of molecular clouds genuinely increases with the local H I column density; this could account for some of the scatter in the $R - \sigma_v$ relation but would imply that Σ_{H_2} and X_{CO} – assuming the average CO brightness temperature is constant – should also increase with $N(\text{H I})$ (see e.g. Dickman et al. 1986; Heyer et al. 2001). A third possibility is that the degree of virialisation in GMCs varies across the LMC, i.e. GMCs in regions with high $N(\text{H I})$ are less gravitationally bound than GMCs in regions with low $N(\text{H I})$, due to the higher external pressure. Provided that the average CO brightness temperature of GMCs in the LMC remains constant, we would also expect the observed value of X_{CO} to increase with $N(\text{H I})$ in this case. Our analysis in Section 6 revealed some evidence for trends between Σ_{H_2} , X_{CO} and $N(\text{H I})$, although the correlations involving the high quality subsample did not satisfy our criteria for significance. There is sufficient scatter in Figures 4 and 7 that none of these explanations can be definitively ruled out.

7.3.3 GMC properties and P_h

Although the MAGMA clouds do not follow the predictions of the E89 molecular cloud model, we find that σ_v and Σ_{H_2} increase with the interstellar pressure (panels [b] and [e] of Fig. 8). These correlations suggest that the external pressure on a GMC in the LMC may indeed play a key role in regulating its dynamical properties, although we caution that we cannot readily distinguish between the role of pressure and shielding in our analysis due to the dominant contribution of Σ_g to our estimate for P_h . The low absolute values of Σ_{H_2} and I_{CO} for the MAGMA clouds imply that their average internal pressure is also low. From the virial theorem, a GMC with $\Sigma_{\text{H}_2} \sim 50 \text{ M}_\odot \text{ pc}^{-2}$ will have internal pressure $P_h/k_B \sim 5 \times 10^4 \text{ K cm}^{-3}$ (e.g. Krumholz & McKee 2005); this is not much greater than the average external kinetic pressure for the MAGMA GMCs, $\langle P_h/k_B \rangle \sim 3.9 \times 10^4 \text{ K cm}^{-3}$, estimated from Equation 10. Plausible optical depth corrections for the H I emission along sightlines towards GMCs (i.e. for τ values between 0.4 and 2) would effectively balance these estimates for the average pressure internal and external to the cloud, although the dense clumpy structure within the GMC would be likely to remain significantly overpressured. A gentle pressure gradient across the molecular cloud boundary may explain why we have found that some properties of the MAGMA clouds are correlated with environmental conditions. It would be interesting to test whether GMCs in nearby spiral galaxies – which have $\langle \Sigma_{\text{H}_2} \rangle \sim 130 \text{ M}_\odot \text{ pc}^{-2}$ (B08) and presumably higher internal pressures relative to the surrounding ISM (see also Krumholz et al. 2009) – exhibit any of the correlations that we have identified for the MAGMA GMCs.

8 CONCLUSIONS

This paper has presented Mopra Telescope observations of $^{12}\text{CO}(J = 1 \rightarrow 0)$ emission from a sample of 125 GMCs in the Large Magellanic Cloud. The data described here were obtained as part of MAGMA, an ongoing mapping survey of the $^{12}\text{CO}(J = 1 \rightarrow 0)$ emission from molecular gas in the Magellanic Clouds. The MAGMA data, which have an angular resolution of 45 arcsec and a spectral resolution of 0.1 km s^{-1} , will be made available to the astronomical community upon completion of the survey, and should be a rich resource for follow-up studies with millimetre and submillimetre facilities on the Atacama Plateau. A discussion of MAGMA’s observational strategy, data products and a final GMC catalogue will be presented in a future paper (Wong *et al.*, in preparation). In this paper, we examined the empirical scaling relations between the basic physical properties of the GMCs in our current LMC cloud list, and dependencies between the cloud properties and the local interstellar environment. We report the following results and conclusions:

1. The observed GMCs have radii ranging between 13 and 160 pc, velocity dispersions between 1.0 and 6.1 km s^{-1} , peak CO brightnesses between 1.2 and 7.1 K, CO luminosities between $10^{3.5}$ and $10^{5.5} \text{ K km s}^{-1} \text{ pc}^2$, and virial masses between $10^{4.2}$ and $10^{6.8} \text{ M}_\odot$. The clouds tend to be elongated, with a median major-to-minor axis ratio of 1.7. These values are comparable to the measured properties of Galactic GMCs. The average mass surface density of the observed clouds is

$\sim 50 M_{\odot} \text{ pc}^{-2}$, approximately half the value determined for GMCs in the inner Milky Way catalogue of Solomon et al. (1987).

2. The MAGMA clouds exhibit scaling relations that are similar to those previously determined for Galactic and extragalactic GMC samples (e.g. Solomon et al. 1987; Bolatto et al. 2008). However the MAGMA LMC clouds are offset towards narrower linewidths and lower CO luminosities compared to GMCs of a similar size in these samples. The scatter in the scaling relations corresponds to order of magnitude peak-to-peak variations in the CO-to-H₂ conversion factor (as inferred from the ratio of the virial mass to the CO luminosity), the H₂ mass surface density and the CO surface brightness of the MAGMA GMCs.

3. The physical properties of star-forming GMCs are very similar to the properties of GMCs without signs of massive star formation. Sightlines through non-star-forming GMCs tend to have lower peak CO brightness, suggesting that the filling fraction and/or brightness temperature of the CO-emitting substructure is lower for clouds without star formation.

4. We find a significant positive correlation between the peak CO brightness and CO surface brightness of the MAGMA clouds and the stellar mass surface density. We propose that these correlations are due to an increase in the CO brightness temperature and/or an increase in the abundance of CO relative to H₂ in the stellar bar region.

5. The velocity dispersion (σ_v) of the MAGMA GMCs increases in regions with high H I column density ($N(\text{H I})$). Higher volume densities and/or higher virial parameters for GMCs in regions with high $N(\text{H I})$ could produce the observed correlation, although the MAGMA data does not provide unambiguous evidence for either of these alternatives.

6. There is some evidence that the H₂ mass surface density of the MAGMA LMC clouds increases with the interstellar kinetic pressure, P_{ext} . Although the molecular cloud model proposed by (Elmegreen 1989) predicts a relation between P_{ext} and the mass surface density of an atomic+molecular cloud complex, the MAGMA clouds do not fulfil the predictions of the model for reasonable values of the metallicity, radiation field and GMC envelope mass.

ACKNOWLEDGMENTS

We thank Christian Henkel, Jonathan Seale and Min Wang for their assistance with MAGMA observations. We also thank staff at the ATNF for observing support, and Robert Gruendl for providing the stellar mass surface density image. We acknowledge extensive use of NASA's Astrophysics Data System Bibliographic Services. TW is supported by NSF grant 08-07323 and the University of Illinois. JO is supported by the National Radio Astronomy Observatory (NRAO) which is operated by Associated Universities, Inc., under cooperative agreement with the National Science Foundation. JLP is supported by an appointment to the NASA Postdoctoral Program at the Jet Propulsion Laboratory, California Institute of Technology, administered by Oak Ridge Associated Universities through a contract with NASA. AH, JPB and DP are grateful to the Australian Research Council for financial assistance during this project via the Linkage International scheme (Australia-France Co-operation Fund in Astronomy). SK is supported in part by the National Research Foundation of Korea (NRF) grant funded by the Korean government (MEST) 2009-0062866. AH thanks Erik Rosolowsky, Adam Leroy, Alberto Bolatto, Kaye Marion and Michael Murphy for helpful discussions. We thank the referee for constructive criticism that improved the analysis in this paper.

REFERENCES

- Akritas M. G., Bershady M. A., 1996, *ApJ*, 470, 706
 Alves D. R., 2004, *New Astronomy Review*, 48, 659
 Babu G. J., Feigelson E. D., 1996, *Astrostatistics*
 Ballesteros-Paredes J., Hartmann L., 2007, *Revista Mexicana de Astronomia y Astrofisica*, 43, 123
 Ballesteros-Paredes J., Klessen R. S., Mac Low M.-M., Vazquez-Semadeni E., 2007, in Reipurth B., Jewitt D., Keil K., eds, *Protostars and Planets V Molecular Cloud Turbulence and Star Formation*. pp 63–80
 Bergin E. A., Hartmann L. W., Raymond J. C., Ballesteros-Paredes J., 2004, *ApJ*, 612, 921
 Bernard J.-P., Reach W. T., Paradis D., Meixner M., Paladini R., Kawamura A., Onishi T., Vijn U. e. a., 2008, *AJ*, 136, 919
 Blanc G. A., Heiderman A., Gebhardt K., Evans N. J., Adams J., 2009, *ApJ*, 704, 842
 Blitz L., 1993, in Levy E. H., Lunine J. I., eds, *Protostars and Planets III Giant molecular clouds*. pp 125–161
 Blitz L., Fukui Y., Kawamura A., Leroy A., Mizuno N., Rosolowsky E., 2007, in Reipurth B., Jewitt D., Keil K., eds, *Protostars and Planets V Giant Molecular Clouds in Local Group Galaxies*. pp 81–96
 Blitz L., Rosolowsky E., 2004, *ApJ*, 612, L29
 Blitz L., Rosolowsky E., 2006, *ApJ*, 650, 933
 Bolatto A. D., Leroy A., Israel F. P., Jackson J. M., 2003, *ApJ*, 595, 167

- Bolatto A. D., Leroy A. K., Rosolowsky E., Walter F., Blitz L., 2008, ArXiv e-prints
- Boulanger F., Abergel A., Bernard J.-P., Burton W. B., Desert F.-X., Hartmann D., Lagache G., Puget J.-L., 1996, *A&A*, 312, 256
- Chieze J. P., 1987, *A&A*, 171, 225
- Chin Y.-N., Henkel C., Whiteoak J. B., Millar T. J., Hunt M. R., Lemme C., 1997, *A&A*, 317, 548
- Cole A. A., Smecker-Hane T. A., Tolstoy E., Gallagher J. S., 2004, in McWilliam A., Rauch M., eds, *Origin and Evolution of the Elements Abundance Patterns of the Large Magellanic Cloud Disk and Bar*
- Dickey J. M., Mebold U., Marx M., Amy S., Haynes R. F., Wilson W., 1994, *A&A*, 289, 357
- Dickman R. L., Snell R. L., Schloerb F. P., 1986, *ApJ*, 309, 326
- Dobashi K., Bernard J.-P., Hughes A., Paradis D., Reach W. T., Kawamura A., 2008, *A&A*, 484, 205
- Elmegreen B. G., 1989, *ApJ*, 344, 306
- Federman S. R., Glassgold A. E., Kwan J., 1979, *ApJ*, 227, 466
- Fleck Jr. R. C., 1988, *ApJ*, 328, 299
- Fukui Y., Kawamura A., Minamidani T., Mizuno Y., Kanai Y., Mizuno N., Onishi T., Yonekura Y., Mizuno A., Ogawa H., Rubio M., 2008, *ApJS*, 178, 56
- Garay G., Johansson L. E. B., Nyman L.-Å., Booth R. S., Israel F. P., Kutner M. L., Lequeux J., Rubio M., 2002, *A&A*, 389, 977
- Gaustad J. E., McCullough P. R., Rosing W., Van Buren D., 2001, *PASP*, 113, 1326
- Hartmann L., Ballesteros-Paredes J., Bergin E. A., 2001, *ApJ*, 562, 852
- Heikkilä A., Johansson L. E. B., Olofsson H., 1999, *A&A*, 344, 817
- Heyer M., Krawczyk C., Duval J., Jackson J. M., 2008, ArXiv e-prints
- Heyer M. H., Brunt C. M., 2004, *ApJ*, 615, L45
- Heyer M. H., Carpenter J. M., Snell R. L., 2001, *ApJ*, 551, 852
- Israel F. P., 1997, *A&A*, 328, 471
- Israel F. P., de Graauw T., Johansson L. E. B., Booth R. S., Boulanger F., Garay G., Kutner M. L., Lequeux J., Nyman L.-A., Rubio M., 2003, *A&A*, 401, 99
- Israel F. P., Johansson L. E. B., Lequeux J., Booth R. S., Nyman L. A., Crane P., Rubio M., de Graauw T., Kutner M. L., Gredel R., Boulanger F., Garay G., Westerlund B., 1993, *A&A*, 276, 25
- Israel F. P., Maloney P. R., Geis N., Herrmann F., Madden S. C., Poglitsch A., Stacey G. J., 1996, *ApJ*, 465, 738
- Johansson L. E. B., Greve A., Booth R. S., Boulanger F., Garay G., de Graauw T., Israel F. P., Kutner M. L., Lequeux J., Murphy D. C., Nyman L.-A., Rubio M., 1998, *A&A*, 331, 857
- Kawamura A., Mizuno Y., Minamidani T., D. Filipović M., Staveley-Smith L., Kim S., Mizuno N., Onishi T., Mizuno A., Fukui Y., 2009, *ApJS*, 184, 1
- Kelly B. C., 2007, *ApJ*, 665, 1489
- Kim S., Staveley-Smith L., Dopita M. A., Freeman K. C., Sault R. J., Kesteven M. J., McConnell D., 1998, *ApJ*, 503, 674
- Kim S., Staveley-Smith L., Dopita M. A., Sault R. J., Freeman K. C., Lee Y., Chu Y., 2003, *ApJS*, 148, 473
- Krumholz M. R., McKee C. F., 2005, *ApJ*, 630, 250
- Krumholz M. R., McKee C. F., Tumlinson J., 2009, *ApJ*, 699, 850
- Kutner M. L., Rubio M., Booth R. S., Boulanger F., de Graauw T., Garay G., Israel F. P., Johansson L. E. B., Lequeux J., Nyman L.-A., 1997, *A&AS*, 122, 255
- Ladd N., Purcell C., Wong T., Robertson S., 2005, *Publications of the Astronomical Society of Australia*, 22, 62
- Larson R. B., 1979, *MNRAS*, 186, 479
- Larson R. B., 1981, *MNRAS*, 194, 809
- Lequeux J., 2005, *The interstellar medium*
- Leroy A., Bolatto A., Stanimirovic S., Mizuno N., Israel F., Bot C., 2007, *ApJ*, 658, 1027
- Leroy A. K., Bolatto A., Bot C., Engelbracht C. W., Gordon K., Israel F. P., Rubio M., Sandstrom K., Stanimirović S., 2009, *ApJ*, 702, 352
- Leroy A. K., Walter F., Brinks E., Bigiel F., de Blok W. J. G., Madore B., Thornley M. D., 2008, *AJ*, 136, 2782
- Luks T., Rohlfs K., 1992, *A&A*, 263, 41
- Mac Low M.-M., Klessen R. S., 2004, *Reviews of Modern Physics*, 76, 125
- MacLaren I., Richardson K. M., Wolfendale A. W., 1988, *ApJ*, 333, 821
- Maloney P., Black J. H., 1988, *ApJ*, 325, 389
- Marx-Zimmer M., Herbstmeier U., Dickey J. M., Zimmer F., Staveley-Smith L., Mebold U., 2000, *A&A*, 354, 787
- McKee C. F., 1989, *ApJ*, 345, 782
- Meixner M., Gordon K. D., Indebetouw R., Hora J. L., Whitney B., Blum R., Reach W., Bernard J.-P. e. a., 2006, *AJ*, 132, 2268

- Minamidani T., Mizuno N., Mizuno Y., Kawamura A., Onishi T., Hasegawa T., Tatematsu K., Ikeda M. e. a., 2008, *ApJS*, 175, 485
- Miville-Deschênes M.-A., Lagache G., 2005, *ApJS*, 157, 302
- Mizuno N., et al., 2001, *PASJ*, 53, 971
- Moorey G. G., Sinclair M. W., Payne J. M., 1997, in Latter W. B., Radford S. J. E., Jewell P. R., Mangum J. G., Bally J., eds, *IAU Symposium Vol. 170 of IAU Symposium*, 3 mm SIS receiver for the Australia Telescope 22 metre Mopra antenna.. pp 441–+
- Nikolaev S., Drake A. J., Keller S. C., Cook K. H., Dalal N., Griest K., Welch D. L., Kanbur S. M., 2004, *ApJ*, 601, 260
- Nikolaev S., Weinberg M. D., 2000, *ApJ*, 542, 804
- Ott J., Wong T., Pineda J. L., Hughes A., Muller E., Li Z., Wang M., Staveley-Smith L., Fukui Y., Weiß A., Henkel C., Klein U., 2008, *Publications of the Astronomical Society of Australia*, 25, 129
- Paradis D., Reach W. T., Bernard J.-P., Block M., Engelbracht C. W., Gordon K., Hora J. L., Indebetouw R., Kawamura A., Meade M., Meixner M., Sewilo M., Vijn U. P., Volk K., 2009, *AJ*, 138, 196
- Pineda J. L., Mizuno N., Stutzki J., Cubick M., Aravena M., Bensch F., Bertoldi F., Bronfman L. e. a., 2008, *A&A*, 482, 197
- Pineda J. L., Ott J., Klein U., Wong T., Muller E., Hughes A., 2009, *ApJ*, 703, 736
- Press W. H., Teukolsky S. A., Vetterling W. T., Flannery B. P., 1992, *Numerical recipes in FORTRAN*, 2nd edn. Cambridge U. Press, Cambridge
- Rosolowsky E., 2007, *ApJ*, 654, 240
- Rosolowsky E., Blitz L., 2005, *ApJ*, 623, 826
- Rosolowsky E., Engargiola G., Plambeck R., Blitz L., 2003, *ApJ*, 599, 258
- Rosolowsky E., Leroy A., 2006, *PASP*, 118, 590
- Sault R. J., Teuben P. J., Wright M. C. H., 1995, in Shaw R. A., Payne H. E., Hayes J. J. E., eds, *Astronomical Data Analysis Software and Systems IV Vol. 77 of Astronomical Society of the Pacific Conference Series*, A Retrospective View of MIRIAD. pp 433–+
- Skrutskie M. F., Cutri R. M., Stiening R., Weinberg M. D., Schneider S., Carpenter J. M., Beichman C., Capps R. e. a., 2006, *AJ*, 131, 1163
- Solomon P. M., Rivolo A. R., Barrett J., Yahil A., 1987, *ApJ*, 319, 730
- Sorai K., Hasegawa T., Booth R. S., Rubio M., Morino J., Bronfman L., Handa T., Hayashi M., Nyman L., Oka T., Sakamoto S., Seta M., Usuda K. S., 2001, *ApJ*, 551, 794
- Staveley-Smith L., Kim S., Calabretta M. R., Haynes R. F., Kesteven M. J., 2003, *MNRAS*, 339, 87
- Strong A. W., Mattox J. R., 1996, *A&A*, 308, L21
- Tasker E. J., Tan J. C., 2008, *ArXiv e-prints*
- Tremaine S., Gebhardt K., Bender R., Bower G., Dressler A., Faber S. M., Filippenko A. V., Green R., Grillmair C., Ho L. C., Kormendy J., Lauer T. R., Magorrian J., Pinkney J., Richstone D., 2002, *ApJ*, 574, 740
- van der Marel R. P., Alves D. R., Hardy E., Suntzeff N. B., 2002, *AJ*, 124, 2639
- van Dishoeck E. F., Black J. H., 1988, *ApJ*, 334, 771
- Walter F., Brinks E., de Blok W. J. G., Bigiel F., Kennicutt R. C., Thornley M. D., Leroy A., 2008, *AJ*, 136, 2563
- Williams J. P., Blitz L., 1998, *ApJ*, 494, 657
- Williams J. P., de Geus E. J., Blitz L., 1994, *ApJ*, 428, 693
- Wilson W. E., Davis E. R., Loone D. G., Brown D. R., 1992, *Journal of Electrical and Electronics Engineering Australia*, 12, 187
- Wolfire M. G., Hollenbach D., Tielens A. G. G. M., 1993, *ApJ*, 402, 195
- Wong T., Blitz L., 2002, *ApJ*, 569, 157
- Wong T., Hughes A., Fukui Y., Kawamura A., Mizuno N., Ott J., Muller E., Pineda J. L., Welty D. E., Kim S., Mizuno Y., Murai M., Onishi T., 2009, *ApJ*, 696, 370
- Yang C.-C., Gruendl R. A., Chu Y.-H., Mac Low M.-M., Fukui Y., 2007, *ApJ*, 671, 374
- Zhao H., Evans N. W., 2000, *ApJ*, 545, L35